Monthly Notices of the ROYAL ASTRONOMICAL SOCIETY

MNRAS **534,** 12–29 (2024) https://doi.org/10.1093/mnras/stae2056
Advance Access publication 2024 September 10

Isotopic abundance of carbon in the DLA towards QSO B1331+170

Dinko Milaković,[1,2]★ John K. Webb [3,4,5]★ Paolo Molaro [1,2] Chung-Chi Lee [5] Prashin Jethwa,[6] Guido Cupani [1,2] Michael T. Murphy [7] Louise Welsh [1,2] Valentina D'Odorico [1,2] Stefano Cristiani [1,2,8] Ricardo Génova Santos,[9,10] Carlos J. A. P. Martins [11,12] Nelson J. Nunes,[13,14] Tobias M. Schmidt [15] Francesco A. Pepe,[15] Maria Rosa Zapatero Osorio,[16] Yann Alibert,[17,18] J. I. González Hernández,[9,10] Paolo Di Marcantonio [2] Enric Palle,[9,10] Rafael Rebolo,[9] Nuno C. Santos,[12,19] Sérgio G. Sousa [12] and Alejandro Suárez Mascareño [9,10]

[1]*Institute for Fundamental Physics of the Universe, Via Beirut, 2, I-34151 Trieste, Italy*
[2]*INAF – Osservatorio Astronomico di Trieste, via Tiepolo 11, I-34131, Trieste, Italy*
[3]*Clare Hall, University of Cambridge, Herschel Rd, Cambridge CB3 9AL, UK*
[4]*Institute of Astronomy, Madingley Road, Cambridge, CB3 0HA, UK*
[5]*Big Questions Institute, Level 4, 55 Holt St., Surry Hills, Sydney, NSW 2010, Australia*
[6]*Department of Astrophysics, University of Vienna, Türkenschanzstraße 17, A-1180, Vienna, Austria*
[7]*Centre for Astrophysics and Supercomputing, Swinburne University of Technology, Hawthorn, Victoria 3122, Australia*
[8]*INFN – National Institute for Nuclear Physics, via Valerio 2, I-34127 Trieste, Italy*
[9]*Instituto de Astrofísica de Canarias, Vía Láctea s/n, E-38200 La Laguna, Tenerife, Spain*
[10]*Departamento de Astrofísica, Universidad de La Laguna, Avenida Astrofísico Francisco Sánchez s/n, E-38206 La Laguna, Tenerife, Spain*
[11]*Centro de Astrofísica da Universidade do Porto, Rua das Estrelas, P-4150-762 Porto, Portugal*
[12]*Instituto de Astrofísica e Ciências do Espaço, CAUP, Rua das Estrelas, P-4150-762 Porto, Portugal*
[13]*Instituto de Astrofísica e Ciências do Espaço, Faculdade de Ciências da Universidade de Lisboa, Campo Grande, P-1749-016 Lisboa, Portugal*
[14]*Departamento de Fisica da Faculdade de Cincias da Universidade de Lisboa, Edifcio C8, P-1749-016 Lisboa, Portugal*
[15]*Observatoire Astronomique de l'Université de Genève, Chemin Pegasi 51, CH-1290 Versoix, Switzerland*
[16]*Centro de Astrobiología (CSIC-INTA), Crta. Ajalvir km 4, E-28850 Torrejón de Ardoz, Madrid, Spain*
[17]*Physikalisches Institut, Space Division, Universität Bern, Gesselschaftsstrasse 6, CH-3012 Bern, Switzerland*
[18]*Center for Space and Habitability, Universität Bern, Gesselschaftsstrasse 6, CH-3012 Bern, Switzerland*
[19]*Departamento de Física e Astronomia, Faculdade de Ciências, Universidade do Porto, Rua do Campo Alegre, P-4169-007 Porto, Portugal*

Accepted 2024 August 29. Received 2024 August 29; in original form 2024 July 25

ABSTRACT

Chemical evolution models predict a gradual build-up of ^{13}C in the Universe, based on empirical nuclear reaction rates and assumptions on the properties of stellar populations. However, old metal-poor stars within the Galaxy contain more ^{13}C than is predicted, suggesting that further refinements to the models are necessary. Gas at high-redshift provides important supplementary information at metallicities $-2 \lesssim$ [Fe/H] $\lesssim -1$, for which there are only a few measurements in the Galaxy. We obtained new, high-quality, VLT/ESPRESSO observations of the QSO B1331+170 and used them to measure ^{12}C/^{13}C in the damped Lyman-α system (DLA) at $z_{\rm abs} = 1.776$, with [Fe/H] $= -1.27$. AI-VPFIT, an artificial intelligence tool based on genetic algorithms and guided by a spectroscopic information criterion, was used to explore different possible kinematic structures of the carbon gas. Three hundred independent AI-VPFIT models of the absorption system were produced using pre-set ^{12}C/^{13}C values, ranging from 4 to 500. Our results show that $^{12}\mathrm{C}/^{13}\mathrm{C} = 28.5^{+51.5}_{-10.4}$, suggesting a possibility of ^{13}C production at low metallicity.

Key words: galaxies: abundances – galaxies: ISM – quasars: absorption lines – quasars: individual: 1331+170.

1 INTRODUCTION

Galaxy formation and chemical evolution models are guided by the observed chemical element abundances in stars of different metallicities and in diffuse gas. Isotopic ratio measurements provide additional constraints, since different isotopes are produced by different nuclear reactions within stellar interiors. Given the similar atomic structure of isotopes, measuring their relative abundances is relatively free from some systematics affecting absolute abundances measurements, such as effects associated with non-local thermal equilibrium, three-dimensional effects in stellar atmospheres, dust depletion, and ionization in diffuse gas. However, the main problem is that one isotope is often much more abundant than the other(s) and their transitions are usually blended, making isotopic abundance ratios difficult to measure.

Due to the large abundance of carbon and the relatively large energy splitting between certain atomic transitions of ^{12}C and ^{13}C, ^{12}C/^{13}C is one of the easier isotopic abundance ratios to measure. ^{12}C is produced by helium-burning inside massive and short lived stars

★ E-mail: jkw.phys@gmail.com (JKW); dinko@milakovic.net (DM)

as a primary element, whilst ^{13}C is produced within intermediate and low-mass stars by the carbon-nitrogen-oxygen (CNO) cycle as a secondary element. As a result, $^{12}C/^{13}C$ is expected to be large ($\gtrsim 1000$) in the early stages of chemical evolution and then decrease with time (Prantzos, Aubert & Audouze 1996; Wiescher et al. 2010; Kobayashi, Karakas & Umeda 2011). Chemical evolution models for the Galaxy predict a slower build-up of secondary elements with time (compared to primary elements), and hence a fast decrease in $^{12}C/^{13}C$ with increasing metallicity (Romano & Matteucci 2003; Kobayashi, Karakas & Lugaro 2020). However, very recent measurements made in stars with [Fe/H] ≈ -4 showed a much lower $^{12}C/^{13}C$ than predicted (Molaro et al. 2023). All such stars have measured $^{12}C/^{13}C < 100$, implying a primary production of ^{13}C at low metallicities that conflicts with the predictions (Kobayashi et al. 2020). In particular, several dwarf stars inexplicably have $^{12}C/^{13}C \lesssim 5$ (Molaro et al. 2023). Such low values are close to the theoretical lower limit of $^{12}C/^{13}C = 4$ imposed by the equilibrium value in the CNO bi-cycle (Caughlan 1965). These new observations suggest that further refinements to chemical evolution models are necessary. In particular, the evolution from very low $^{12}C/^{13}C$ values at low metallicities to measured solar values ($^{12}C/^{13}C = 91 \pm 1.3$; Goto et al. 2003; Ayres et al. 2013) remains unexplained.

Unfortunately, there are only a few $^{12}C/^{13}C$ measurements in the range $-3 <$ [Fe/H] < -0.2 (Kobayashi et al. 2020). Gas at high-redshift can provide important supplementary information in a metallicity regime for which there is no information in the Galaxy. Few measurements or limits exist at cosmological distances (seven measurements are tabulated in Romano 2022 with $z_{abs} \geq 0.7$, with one further more recent measurement from Welsh et al. 2020). Rotational transitions of molecular gas were used to measure isotopic ratios of several elements, including C, (e.g. Muller et al. 2006; Henkel et al. 2010, 2014; Wallström, Muller & Guélin 2016; Noterdaeme et al. 2017). Atomic transitions associated with damped Lyman-α (DLA) absorption systems have also been used to constrain $^{12}C/^{13}C$ (e.g. Levshakov et al. 2006; Carswell et al. 2011; Welsh et al. 2020).

Here, we report on $^{12}C/^{13}C$ in the DLA at $z_{abs} = 1.776$ towards the quasar QSO B1331+170, also known as QSO J1333+1649 (RA $13^h33^m35\overset{s}{.}78$, Dec. $+16°49'04\overset{''}{.}014$, J2000). This quasar ($V = 16.6$ mag, $z_{em} = 2.08895$) was first spectroscopically observed by Baldwin et al. (1973) and the DLA was first characterized by Strittmatter et al. (1973) and Carswell et al. (1975). Meyer et al. (1986) used the neutral carbon transitions in this DLA to make the first measurements of the cosmic microwave background radiation temperature, T_{CMB}, at high redshift, with later refinements by Songaila et al. (1994), Cui et al. (2005), and Carswell et al. (2011). Carswell et al. (2011) was the first to constrain $^{12}C/^{13}C$ in this system, finding it must be >5 (at 2σ confidence limit, CL). Here, we present a new $^{12}C/^{13}C$ constraint derived from new high spectral resolution, high signal-to-noise ratio (S/N), observations with the Echelle SPectrograph for Rocky Exoplanets and Stable Spectroscopic Observations (ESPRESSO; Pepe et al. 2021) on the ESO Very Large Telescope (VLT). A T_{CMB} measurement from the same observations as are used in this paper will be reported in a separate paper.

2 DATA

2.1 ESPRESSO observations

ESPRESSO is an optical (380 to 790 nm) Echelle spectrograph mounted on the VLT, that can be fed by the light of any one of VLT's four Unit Telescopes. Its high-spectral resolution, [$R = \lambda/\Delta\lambda = 140000$, where $\Delta\lambda$ is the full width at half-maximum (FWHM) of the resolution element], ensures that contributions to the absorption profile shapes from ^{12}C and ^{13}C can be sufficiently resolved, and its wavelength calibration allows individual exposures to be combined with precision of several m s^{-1} (Schmidt et al. 2021). ESPRESSO's optomechanical design is intended to ensure that the recorded spectrum does not depend on seeing conditions and that small guiding errors do not cause spectral shapes to vary, thus potentially emulating the presence of ^{13}C. However, ESPRESSO's wavelength coverage provides access only to two C I transitions (λ1560 and λ1657, where the wavelengths are in units Å) of the five known in this DLA (others being λ1277, λ1280, and λ1328).

We used ESPRESSO in its 'singleHR' mode, with one of its two fibres (A) positioned on the object and the second fibre (B) on an empty position 7 arcsec away for better sky subtraction. Observations were spread across 4 yr, with 12 observations taken in 2019, 11 observations in 2021, and 9 observations in 2023, for a total exposure time of 41.1 h. The observing log is given in Table 1, where we have grouped the observations into three epochs (I–III) for easier referencing later in the text. Note that the pixel binning used during

Table 1. A summary of observations used in this work. The columns provide information on the observing time, detector pixel binning mode (spatial × spectral direction), exposure time in seconds, airmass at the end of the observations, and VLT Unit Telescope (UT) used, in that order.

Observing time (UTC)	Binning (X×Y)	T_{exp} (s)	Airmass	Telescope
Epoch I				
2019-04-27T01:30:59.145	2 × 1	5400	1.38	UT3
2019-04-27T03:02:07.350	2 × 1	5400	1.35	UT3
2019-04-28T03:47:39.546	2 × 1	3802	1.38	UT3
2019-04-29T01:15:53.547	2 × 1	5400	1.39	UT3
2019-04-29T02:46:56.186	2 × 1	6900	1.38	UT3
2019-05-02T01:09:26.902	2 × 1	6800	1.35	UT3
2019-05-02T03:03:55.049	2 × 1	6100	1.41	UT3
2019-05-03T01:01:56.418	2 × 1	6800	1.35	UT3
2019-05-03T02:56:24.560	2 × 1	6200	1.40	UT3
2019-05-04T00:54:24.533	2 × 1	6800	1.36	UT3
2019-05-04T02:48:52.709	2 × 1	6800	1.42	UT3
2019-05-05T02:54:59.102	2 × 1	6600	1.43	UT3
Epoch II				
2021-03-08T07:08:10.623	4 × 2	3900	1.39	UT3
2021-03-08T08:13:54.843	4 × 2	3900	1.61	UT3
2021-03-10T06:56:55.242	4 × 2	4380	1.40	UT3
2021-03-10T08:10:33.381	4 × 2	4380	1.69	UT3
2021-03-18T06:06:23.381	4 × 2	4100	1.36	UT1
2021-03-18T07:15:23.208	4 × 2	4100	1.54	UT1
2021-03-18T08:24:21.701	4 × 2	4100	2.02	UT1
2021-03-19T05:01:59.645	4 × 2	4100	1.33	UT1
2021-03-19T06:10:58.690	4 × 2	4100	1.37	UT1
2021-03-19T07:19:58.152	4 × 2	4100	1.58	UT1
2021-03-19T08:28:59.043	4 × 2	3133	1.95	UT1
Epoch III				
2023-02-20T07:12:08.210	4 × 2	3400	1.33	UT3
2023-02-20T08:15:22.487	4 × 2	3400	1.38	UT3
2023-02-21T07:54:52.027	4 × 2	3400	1.35	UT1
2023-02-22T06:47:31.746	4 × 2	3400	1.34	UT1
2023-02-22T07:48:27.689	4 × 2	3440	1.35	UT1
2023-02-23T07:01:45.443	4 × 2	3400	1.33	UT2
2023-02-24T06:44:28.982	4 × 2	3440	1.34	UT1
2023-02-25T06:06:12.773	4 × 2	3400	1.37	UT1
2023-02-25T07:06:26.681	4 × 2	3400	1.33	UT1

detector read-out was 2 × 1 (X×Y, spatial × spectral direction) in epoch I and 4 × 2 in epochs II and III.

2.2 Data reduction, wavelength calibration, and sky subtraction

Observations were processed using ESPRESSO Data Reduction Software (DRS) version 3.0.0 (Modigliani, Sosnowska & Lovis 2023), adopting default parameters for all recipes except for the sky subtraction, which was smoothed instead of pixel-by-pixel. The DRS removes detector effects and cosmic rays, and extracts the scientific and the sky spectra from the raw frames using a modified version of the optimal extraction algorithm (Horne 1986; Robertson 1986), as described in Zechmeister, Anglada-Escudé & Reiners (2014). The extracted spectra are then corrected for the instrument pixel-to-pixel variations before being wavelength calibrated. ESPRESSO provides two wavelength calibration sources: a laser frequency comb (LFC) and thorium-argon (ThAr) arc lamp imaged simultaneously with a Fabry–Pérot etalon. For the majority of our observations, the LFC was unavailable or did not cover the two C I transitions targeted for this analysis so ThAr + Fabry–Pérot etalon frames were used to calibrate the spectra presented here. In the final step, a 100 pixel wide sliding average of the sky spectrum is subtracted from the science spectrum.

2.3 Spectral combination and continuum estimation

UVES_POPLER version 1.05 (Murphy 2018; Murphy et al. 2019) was used to produce the combined spectrum from reduced observations. UVES_POPLER defines a new (log-linear) wavelength grid on to which it redisperses the individual spectra and calculates the inverse-variance weighted average of the values falling within each pixel of the new wavelength grid. Observations taken within a single epoch were combined into a single spectrum, with a wavelength increment of 0.4 km s^{-1} (0.8 km s^{-1}) for observations taken with 2 × 1 (4 × 2) detector binning. In producing the combined spectrum, UVES_POPLER leverages the availability of the large number of independent flux estimates in each pixel to remove outlying flux values and clip any remaining cosmic rays. UVES_POPLER also produces a continuum estimate by fitting a sixth order Čebyšëv polynomial over 2500 km s^{-1} wide chunks of the combined spectrum.

2.4 Removing contaminants

2.4.1 Blends with sky lines and systems at other redshifts

No sky lines were found to blend with C I transitions at $z_{\rm abs} = 1.776$. Carswell et al. (2011) reported several transitions at other redshifts in their proximity. Al IIIλ1854 at $z_{\rm abs} = 1.329$ coincides with the expected positions of C I* transitions in the proximity of λ1560, and Fe Iλ2484 at $z_{\rm abs} = 0.7444$ is nearby. To eliminate any impact from these blends, we set the spectral error array in the wavelength ranges 4331.4575 Å ≤ λ ≤ 4331.8086 Å (Al III) and 4333.5781 Å ≤ λ ≤ 4333.7446 Å (Fe I) to 1000, effectively removing these wavelength ranges from consideration. Our ESPRESSO data does not provide evidence for the existence of the previously reported (Carswell et al. 2011) blend between C Iλ1657 at $z_{\rm abs} = 1.776$ and C IVλ1550 at $z_{\rm abs} = 1.9662$.

2.4.2 Flux artefacts

Upon combining epoch I spectra, we discovered the unexplained presence of numerous weak but statistically significant flux artefacts in the spectrum. Their presence was first reported in the ESPRESSO spectrum of the quasar HE0515−4414 (Murphy et al. 2022). The artefacts appear as weak (a few per cent), positive or negative departures from the average of the surrounding flux values. A typical artefact spans several km s^{-1}, appearing at the same (or very similar) positions in the spectrum in each exposure such that traditional outlier rejection methods and spectral combination procedures (as implemented in UVES_POPLER) resulted in the increased statistical significance of the artefacts instead of their removal.

Comparing the three epoch spectra with each other (and other quasar spectra we obtained), we saw that the positions of the artefacts in each epoch spectrum correlated with Earth's motion with respect to the Solar system barycentre, indicating an origin that is fixed in the laboratory rest frame (see fig. 2 of Pasquini & Milaković 2024). The artefacts' origin were tracked to clusters of 'warm' detector pixels, that is pixels which erroneously trap an excess of electrons, but which evade detection in hour-long dark exposures in the default DRS settings. We identified two warm pixel patches in the proximity of transitions of interest: one in between 4330.93 and 4331.14 Å, and another in between 4600.94 and 4601.08 Å (wavelengths in the Earth laboratory rest frame). These wavelength ranges were appropriately shifted to the Solar system barycentre and masked in all 32 individual spectra, which were then combined as previously described. The final S/N is reported in Table 2.

Table 2. S/N per pixel in the continuum for co-added observations. The first column identifies the observation epoch (or their combination), whilst the second column gives the pixel size (in km s^{-1}). The last two columns give the S/N values for the two C I transitions studied here. Note that the values listed for epochs I–III do not simply add in quadrature to produce the combined epoch I+II+III value since spectral dispersions differ.

Epoch	Pixel size (km s^{-1})	Transition λ1560	Transition λ1657
I	0.4	32	37
II	0.8	38	41
III	0.8	38	40
I + I + III	0.8	70	78

3 AI-VPFIT MODELS

This work leverages the recently developed spectral analysis tool AI-VPFIT to perform a more comprehensive exploration of the uncertainties (Webb et al. 2021; Lee et al. 2021a, b, 2023; Webb, Lee & Milaković 2022), which expands upon ideas first introduced in GVPFIT (Bainbridge & Webb 2017a, b). Previous to this work, limits on ^{13}C abundances were set by examining how χ^2 changes after a specific quantity of ^{13}C has been added into a model of the absorption system containing ^{12}C only (Levshakov et al. 2006), or by checking how much ^{13}C can be accommodated by the data through simulations of spectra with the same characteristics as the observations (Carswell et al. 2011; Welsh et al. 2020).

Given an observed spectrum, AI-VPFIT uses artificial intelligence methods to produce a model for the data, relying on genetic algorithms in combination with a spectroscopic information criterion (SpIC; Webb et al. 2021) to guide the modelling process. SpIC penalizes the retention of model parameters fitting weak features more heavily than it penalizes parameters fitting strong features. The validity of this modelling system, in terms of obtaining unbiased parameter estimates, has been examined in some detail using simulated spectra by Lee et al. (2021a) and Webb et al. (2022). The simulated spectra were fitted using AI-VPFIT to compare input and estimated

parameter values, finding that AI-VPFIT provides robust and unbiased estimates. This is as expected, since VPFIT (Carswell & Webb 2014) is embedded within AI-VPFIT, the former being an extensively tested system. Further, spectral models constructed using SpIC retrieved parameter values more accurately than those guided by the corrected Akaike Information Criterion (Akaike 1974; Hurvich & Tsai 1989) or the Bayesian Information Criterion (Bozdogan 1987).

Starting from a single-component model in the first generation, AI-VPFIT increases the number of absorbing components in each generation by trying out a user-specified number of trials for additional components (eight in our case) and choosing the one that minimizes SpIC. Positions at which the new components are tried is fully determined by a (user specified) seed for the random number generator, making the whole process fully reproducible. This process ends when a set number of attempts fail to further minimize SpIC (30 in our case). AI-VPFIT then performs small adjustments to the model by including modifications to the continuum estimate and tests whether all of the components are necessary (on the basis of SpIC). AI-VPFIT is also capable of identifying blends with unidentified species (interlopers). Having removed known contaminants in Section 2.4, the option of using interlopers was turned off to remove the possibility of fitting real ^{13}C absorption in this way. Further details on AI-VPFIT procedures are given in Lee et al. (2021a).

AI-VPFIT was used to produce three hundred independent spectral models to determine χ^2 as a function of assumed ^{13}C abundance in the spectrum and to take into account uncertainties associated with slightly different kinematic structures caused by model non-uniqueness. This was not done before since interactive analysis by a human modeller is time-consuming. AI-VPFIT also allows for examining any biases that may be present by first constructing a model containing ^{12}C only and to explore the impact of model non-uniqueness on the final result (Lee et al. 2021b; Webb et al. 2022).

3.1 Resolution and instrumental profile

Theoretical absorption system models are convolved with the assumed shape of ESPRESSO's instrumental profile (IP) before calculating the descent direction in model parameter space. Empirical ESPRESSO IP models were not available at the time, so the IP was approximated to be Gaussian in shape. The resolution for the Gaussian profiles was determined from LFC calibration frames, again available in epoch III, with an extended wavelength range that covers also the two C I transitions of interest. The FWHM was determined in all locations at which the two C I transitions appear. The final FWHM values used inside AI-VPFIT were their average values: $v_{\rm FWHM}(\lambda1560) = 2.362$ and $v_{\rm FWHM}(\lambda1657) = 2.341$ km s^{-1}. Our results are insensitive to small uncertainties on the FWHM values used. For one of the models produced, we explored how best-fitting parameters change when the FWHM is changed by ±1 per cent (based on typical variations seen in LFC calibration frames). We found that model parameter values changed by $\ll 1\sigma$, where σ here denotes their uncertainties derived from the covariance matrix at best fit.

3.2 Setting up the calculations

The calculations were set-up to step through $\mathcal{R} \equiv {}^{13}\mathrm{C}/{}^{12}\mathrm{C}$ to avoid mathematical infinities associated with low ^{13}C abundances. All AI-VPFIT calculations were set-up in exactly the same way, except for the assumed $\mathcal{R}$, which varied from 0.002 to 0.25 in 100 logarithmic steps (sampling was denser at low $\mathcal{R}$). The upper limit on $\mathcal{R}$ is set by the CNO bi-cycle (Caughlan 1965). Three different seeds for the random number generator were used for each $\mathcal{R}$ value, for a total of 300 models.

Table 3. Atomic data for transitions used in this work. The columns give the atomic species, the atomic mass, the laboratory measured wavelength, the laboratory oscillator strength, and the natural damping constant Γ, in that order. AMU stands for atomic mass unit. Empty fields should be interpreted as repeated entries from one line above. All oscillator strengths are from Goldbach & Nollez (1987) and all Γ values are from Li et al. (2000). Wavelengths for C Iλ1560 are from Haridass & Huber (1994) and for λ1657 are from Lai et al. (2020).

Species	Atomic mass (AMU)	Wavelength (Å)	$f^{\rm lab}$	Γ (S^{-1})
C I	12.0	1560.3092	0.077400	1.27×10^8
	13.0	1560.2920		
C I**	12.0	1560.6823	0.058100	1.27×10^8
	13.0	1560.6650		
C I**	12.0	1560.7091	0.019300	1.27×10^8
	13.0	1560.6920		
C I*	12.0	1561.3402	0.011600	1.27×10^8
	13.0	1561.3220		
C I*	12.0	1561.3667	0.000772	1.27×10^8
	13.0	1561.3500		
C I*	12.0	1561.4385	0.064900	1.27×10^8
	13.0	1561.4240		
C I**	12.0	1656.2667	0.062100	3.61×10^8
	13.0	1656.2695		
C I	12.0	1656.9277	0.149000	3.60×10^8
	13.0	1656.9308		
C I*	12.0	1657.0077	0.111000	3.61×10^8
	13.0	1657.0104		
C I**	12.0	1657.3788	0.037100	3.60×10^8
	13.0	1657.3812		
C I**	12.0	1657.9068	0.049400	3.60×10^8
	13.0	1657.9096		
C I*	12.0	1658.1206	0.037100	3.61×10^8
	13.0	1658.1234		

Information on the ratio was provided to AI-VPFIT through the 'atom.dat' file, containing laboratory wavelengths, oscillator strengths, and natural damping constants (Γ) for the transitions (see Table 3). This file was modified in two ways. First, all ground state atomic transitions originating either in ^{12}C or in ^{13}C were labelled simply as C, such that inserting a C component would automatically result in absorption from both isotopes. The same was also done for C I* and C I**, the fine-structure states. Secondly, all oscillator strengths f for the relevant transitions were modified according to the equations:

$$f^{\rm modified}({}^{12}\mathrm{C}) = x f^{\rm lab}, \quad (1)$$

$$f^{\rm modified}({}^{13}\mathrm{C}) = (1-x) f^{\rm lab}, \quad (2)$$

where $x = {}^{12}\mathrm{C}/\mathrm{C} = 1/(1+\mathcal{R})$ and the superscript lab refers to the measured laboratory value (see Table 3).

Provided with the modified 'atom.dat', AI-VPFIT is able to produce a model for the observations with a pre-determined $\mathcal{R}$. In producing the models, the three epoch spectra were kept separate, and all C species were required to be present in all components with their redshifts tied together. Column densities of the tied C I, C I*, and C I** were independent free parameters. A trivial constraint (for numerical convenience) was imposed such that the minimum column density N allowed for any species was $\log(N/\mathrm{cm}^{-2}) = 7.99$. This value is well below any detection threshold in our data and hence has no impact on the results obtained. ^{12}C and ^{13}C were assumed to have

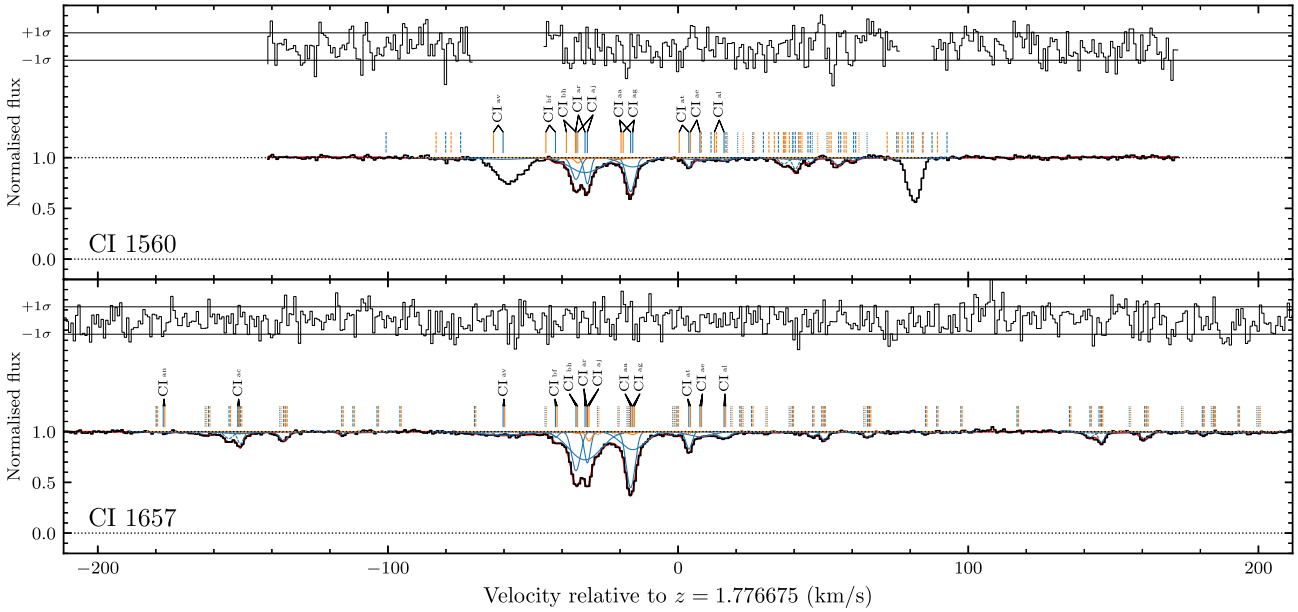

Figure 1. ESPRESSO spectrum of QSO B1331+170 in the wavelength region of the two C I transitions studied here (indicated in the bottom left corner of each panel). The black histogram is the summed spectrum from all three epochs with 0.8 km s^{-1} wide pixels (Fig. A1 shows the individual epoch spectra). The solid red line going through the spectrum shows a 12-component AI-VPFIT model with an assumed ^{12}C/^{13}C = 28.14, close to the final value derived in Section 4. The model has $\chi^2_\nu = 0.6362$. Tick marks above the data show the positions of individual components in the model, with blue and orange ticks showing ^{12}C and ^{13}C, respectively. Continuous solid tick marks show ground state transitions (which are the only ones labelled), whereas dashed and dotted ticks show the fine-structure transitions (C I* and C I**, respectively). The thin black histogram above the spectrum shows the normalized residuals (data − model)/error. Missing residuals seen in λ1560 transition indicate spectral regions contaminated by transitions at other redshifts (Al III λ1854 at $z_{\rm abs} = 1.329$ is at −60 km s^{-1} and Fe I λ2484 at $z_{\rm abs} = 0.7444$ is at +80 km s^{-1}), which were not modelled. Thin horizontal black lines indicate ±1σ ranges. Labels for all transitions are provided in another figure included as supplementary material.

the same line widths, i.e. fully turbulent broadening was imposed. We return to this approximation in Section 6. For similar reasons of numerical convenience, the smallest allowed Doppler b-parameter was 0.03 km s^{-1}, $\lesssim 10$ per cent of the pixel size. None of our AI-VPFIT models contain components with b-parameters near this limit (the smallest was three times larger).

3.3 Quality check of the models

Fig.1 shows one of the AI-VPFIT models with 12 velocity components. Fig. 2 shows the number of components (N_C) for all models as a function of $\mathcal{R}$, with a corresponding histogram. No models have been produced with fewer than 9 or more than 16 components, with the median number of components being 12. Interestingly, while models with $N_C = 9$ to 14 were produced over a wide range of $\mathcal{R}$ values, the two models with $N_C = 15$ and the one model with $N_C = 16$ are associated only with high $\mathcal{R}$. Examining the latter three models revealed them not to fit well the strong feature at −17 km s^{-1} in C I λ1657 (the residuals systematically deviate from zero), so they were discarded.[1] Similarly, all three models with $N_C = 9$ were found to erroneously fit the 'double' absorption feature (located between −30 and −36 km s^{-1} in Fig. 1) using a single component, and were also discarded. Visual examination of the remaining models did not show obvious problems with fitting the observations. We show several other models in Appendix A. Plots of all models are available as online supplementary material.

[1]The $(\mathcal{R}, \chi^2)$ values of these models are (0.215973,2093.7281), (0.226768,2100.352), and (0.250001,2114.7071), i.e. they are marked by the three crosses sitting below the black points in the top panel of Fig. 3.

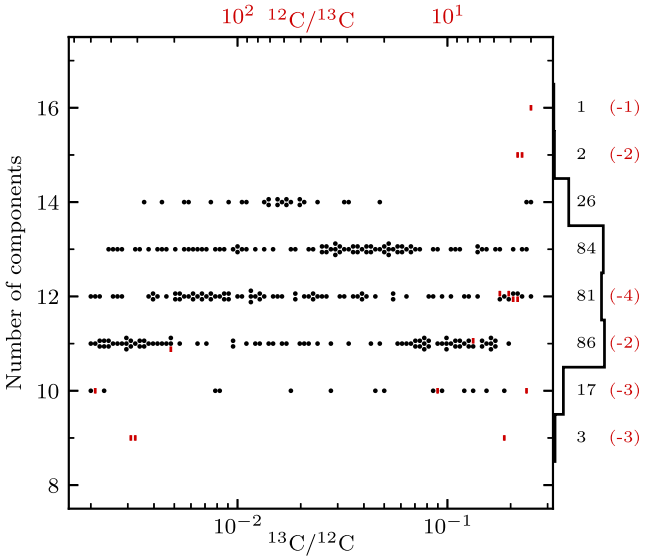

Figure 2. Number of C components, N_C, for the 300 AI-VPFIT models with a histogram. Three models are produced at each $\mathcal{R}$, so multiple models with the same N_C are vertically offset from each other for clarity and visual effect. The total number of models in each group is indicated to the right, where the red numbers in brackets state how many models were removed from the analysis (see the text). Removed models are shown as short vertical red lines in the main panel. Ticks in the bottom with black labels show the ^{13}C/^{12}C, and ticks on the top with red labels show ^{12}C/^{13}C.

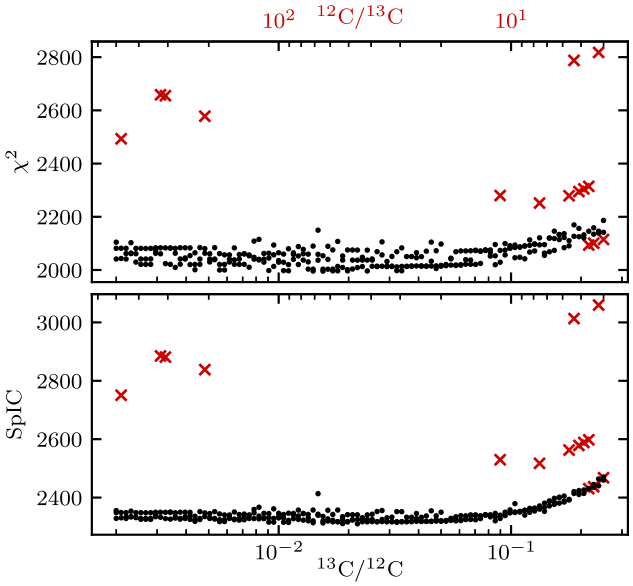

Figure 3. χ^2 (top panel) and SpIC (bottom panel) for the 300 AI-VPFIT models, as a function of $^{13}C/^{12}C$ (bottom ticks and black labels) or $^{12}C/^{13}C$ (top ticks and red labels) on a logarithmic scale. Black dots are the 285 points used in the analysis and 15 models plotted as red crosses have been discarded (see the text).

Also interesting is the apparent preference towards models with a specific N_C for a given $\mathcal{R}$. For example fewer components are generally required when $\mathcal{R}$ is assumed to be at either extreme of the examined range. Models requiring the largest number of components (14) prefer $\mathcal{R}$ between 0.01 and 0.02, and do not spread in $\mathcal{R}$ like all the others (ignoring the 2 points at high $\mathcal{R}$). $N_C = 13$ models seem to preferentially appear between $\mathcal{R} \approx 0.02$ and 0.08 and models with $N_C = 12$ do not appear to cluster significantly at any $\mathcal{R}$ value. $N_C = 11$ models are preferred for two $\mathcal{R}$ ranges: between 0.07 and 0.2, and below 0.005. This split is suggestive of different velocity structures and hence model non-uniqueness. On the other hand, $N_C = 10$ appear at all $\mathcal{R}$ values but are not very common.

The top panel of Fig. 3 shows the χ^2 for all 300 models, calculated as:

$$\chi^2 = \sum_{i=1}^{N} \left(\frac{F_i - \mathcal{F}_i}{\sigma_i} \right)^2 . \quad (3)$$

Above, F_i is the observed flux in the ith pixel, $\mathcal{F}_i$ is its model predicted value, and σ_i is the observed flux error estimate (in our case, the root-mean-square array produced by UVES_POPLER was used in place of the spectral variance array produced by the pipeline, for details see Murphy et al. 2019). The bottom panel of the same Figure shows SpIC = χ^2+ a penalty term that is a function of model parameters (Webb et al. 2021), with the penalty term being different for each model. We note the smaller scatter in SpIC compared to χ^2, a general trend seen before in Lee et al. (2021b). See further comments in Section 4.3. The smallest χ^2 and SpIC values appear between $\mathcal{R} = 0.01$ and 0.04, corresponding to $^{12}C/^{13}C$ between 25 and 100.

12 models show anomalously large χ^2 values (3, 3, 2, 4 models with $N_C = 9, 10, 11, 12$, respectively, some of which were previously identified as problematic). These models were also rejected. The reduced $\chi^2_\nu \equiv \chi^2/\nu$ (ν being the number of degrees of freedom) of the 285 models ranges between 0.621 and 0.678, with 0.638 being the median value. These values are clearly slightly below the expectation of around unity. The reason is well-understood: re-dispersion of spectra and their subsequent combination create adjacent pixel correlations in the combined spectrum. Parameter error estimates take this into account, as described in Carswell (2023). Since the spectra from three epochs were kept as separate entities during the modelling, we spot-checked for consistency (goodness-of-fit) for each epoch. In cases examined, the χ^2 values for corresponding regions were fully consistent, i.e. the overall model fitted each epoch equally well.

3.4 Inter-model variation and non-uniqueness

As described above, a large number of models were computed. We used 100 different settings for $^{12}C/^{13}C$, and at each $^{12}C/^{13}C$ compute three independent AI-VPFIT models. At fixed $^{12}C/^{13}C$, each of the three models is constructed independently, in the sense that trial absorption component placement is random within the fitting range. Model development therefore proceeds differently each time. This emulates, in a rather natural way, the notion of using a large number of independent interactive modellers, and hence avoids bias. The consequence of this is that slight variations from one model to the next are seen in the ensemble of AI-VPFIT models. We illustrate this in Fig. 4 by showing both the astronomical data and the 285 surviving models (see Section 3.3) superimposed. Tick marks show the positions of velocity components for all 285 models, for the dominant section of the absorption system (compare Figs 1 and 4). The colour coding provides further information, since it shows the $^{12}C/^{13}C$ for each model. In Fig. 4, one must appreciate that not all components illustrated are present in all models. For example one AI-VPFIT model might opt to use a single velocity component whilst another might prefer to use two weaker ones. The summed optical depths over all models shown therefore is not intended to represent a good fit to the astronomical data, but is instead intended to illustrate model variation.

There are at least three important features for constraining $^{12}C/^{13}C$: at –38, –20, and +4 km s^{-1}. $^{12}C/^{13}C$ is not allowed to be too high, otherwise there will be excess absorption in the blue wing of C Iλ1560 at –38 km s^{-1}. A low $^{12}C/^{13}C$ would result in insufficient absorption at –20 km s^{-1} in C Iλ1560, but a high $^{12}C/^{13}C$ would cause the model to fall below the data. In the +4 km s^{-1} ^{12}C feature, some ^{13}C is needed in λ1560 to fit weak absorption at +1 km s^{-1} and similarly at +5 km s^{-1} in λ1657. Interestingly, the feature at +4 km s^{-1} is the only one that is consistently fitted by a single component in all 285 models. Determining which of these three features provides the most stringent constraint is not easy. Isolating any particular component to investigate that component's relative importance in constraining the overall $^{12}C/^{13}C$ is difficult; artificially freezing some parameters whilst allowing others to vary is likely to make error estimates for parameters of interest unreliable. Irrespective, as Fig. 4 shows, several velocity components contribute to the overall constraint.

The 'AI-Monte Carlo' approach used in this work allows us to examine, in detail, model non-uniqueness, which can be seen visually in Fig. 4. It is interesting that the AI-VPFIT models of ESPRESSO data are in broad agreement with previous measurements for the physical characteristics of the gas by Carswell et al. (2011), although the improvement in spectral resolution offered by ESPRESSO means far more components are resolved. Further details can be found in Appendix B. In the following Section, we develop methods to simultaneously use the set of model calculations in order to place simple constraints on the $^{12}C/^{13}C$ averaged over the absorption

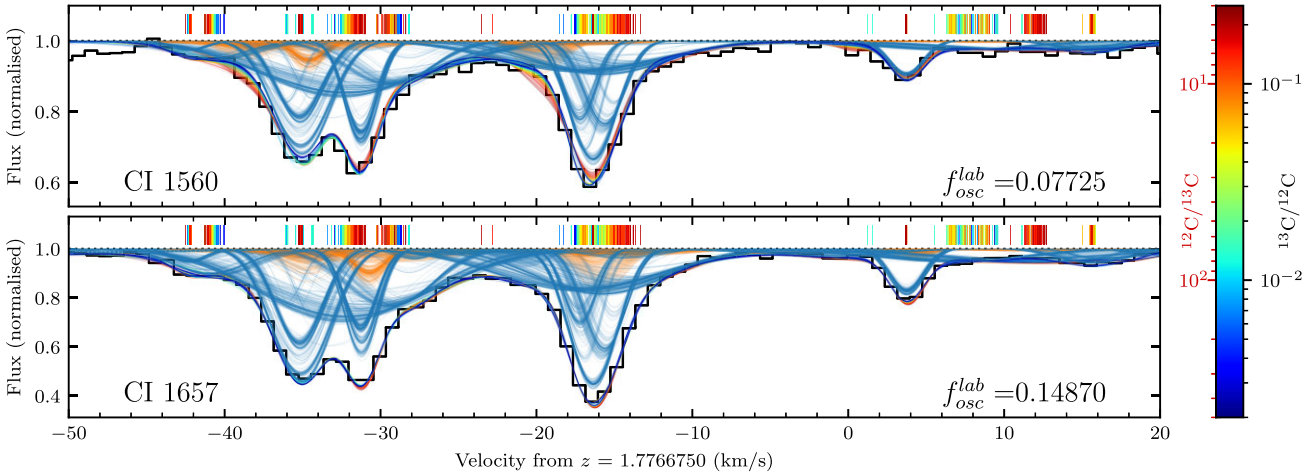

Figure 4. Illustration of model variation and non-uniqueness. The astronomical data are shown as a black histogram (combined epochs I+II+III, 0.8 km s^{-1} wide bins). Individual models are shown as coloured lines, with their colour corresponding to a specific ^{12}C/^{13}C value, as per the colour bar to the right. Coloured tick marks show the positions of ^{12}C absorption in those models (also as per the colour bar). There are 2542 C I components shown from all 285 models (more components fall outside the plotted velocity range, but they fit weaker absorption features). Thin blue lines show ^{12}C absorption and thin orange lines show ^{13}C absorption after convolution with the assumed IP. Not all components seen in the Figure are present in all models (see Section 3.4). Note the different ordinate scales for the two panels.

complex. We also show how, in this particular case, non-uniqueness turns out to create 'groupings' in ^{12}C/^{13}C space.

4 ANALYSIS

The likelihood of $\mathcal{R}$ is:

$$\mathcal{L}(\mathcal{R}) = \exp\left[-\frac{1}{2}\chi^2(\mathcal{R})\right]. \quad (4)$$

χ^2 minimizes ($\mathcal{L}$ maximizes) for the physically correct $\mathcal{R}$, and can be approximated by a parabola around that value:

$$\chi^2(\mathcal{R}) \approx a(\mathcal{R} - \mathcal{R}_{\rm min})^2 + \chi^2_{\rm min}, \quad (5)$$

where a defines the parabola's openness, and $\mathcal{R}_{\rm min}$ and $\chi^2_{\rm min}$ are the vertex coordinates. The χ^2 values of the 285 models are assumed to scatter normally around equation (5) prediction with variance ς^2. Equation (4) must be regarded as an approximation because the terms in the χ^2 summation are not independent.

4.1 Dividing the models into five subsets

Fig. 5 shows there is a clear stratification in χ^2, most of which can be attributed to the number of free model parameters, that is to the number of carbon components in the model (N_C). There is also a possible bifurcation for models with the same N_C: models at similar $\mathcal{R}$ appear systematically offset in χ^2 by approximately the same amounts, apparently grouping together. Models with N_C = 11, 12, and 13 (red squares, blue triangles, and green diamonds, respectively) show this effect most clearly. Comparison of models and their parameters did not reveal any clues on the origin of this effect.

χ^2 values were divided into subsets according to their N_C, and were henceforth treated independently. The five groups are shown by symbols of different colours in Fig. 5. Parabola parameters (and their uncertainties) for each subset were determined using Monte Carlo Markov Chain (MCMC) calculations (implemented in NUMPYRO; Phan, Pradhan & Jankowiak 2019) such that the uncertainties can be propagated into constraints on $\mathcal{R}$. Parameters a, $\chi^2_{\rm min}$, and $\mathcal{R}_{\rm min}$ were all sampled from uniform prior distributions

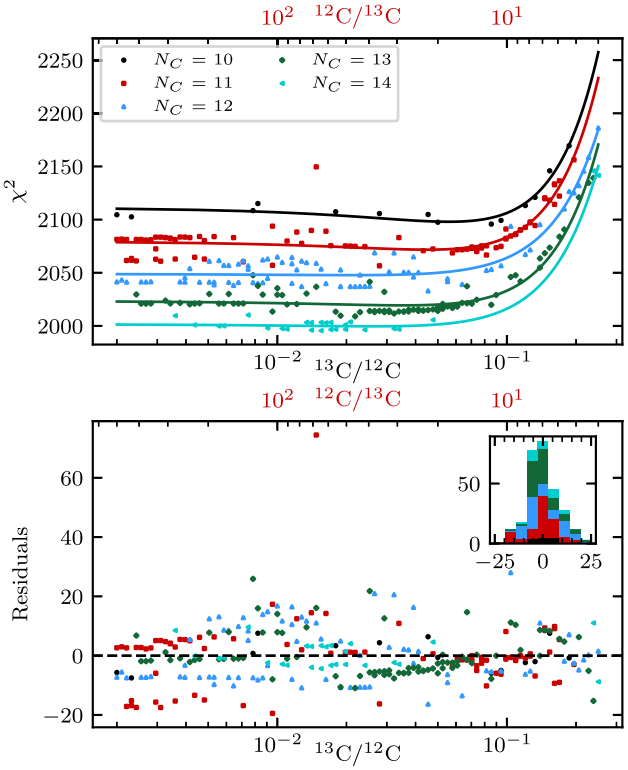

Figure 5. Results of MCMC fitting of equation (5) to observed χ^2 values, subdivided according to N_C. *Top panel*: Coloured symbols are 285 models and the coloured lines are the best-fitting parabolas going through them. Parabola parameters are independent from each other. *Bottom panel*: Residuals (data−model) of the fits shown in the top panel. Some apparently correlated structures remain (see the text). The inset shows a stacked histogram of the residuals. In both panels, ticks in the bottom with black labels show the ^{13}C/^{12}C, and ticks on the top with red labels show ^{12}C/^{13}C.

having the following ranges: (2000,5000), (1900,2200), (0,0.25), in the same order. ς was independently determined for all five subsets, having an exponential distribution prior with a scale of unity. 10 MCMC chains were ran with 7000 warm-up steps and 2500 sample steps. Convergence was assessed using two diagnostics: the split Gelman–Rubin $\hat{R}$ (Vehtari et al. 2021) and effective sample size $N_{\rm eff}$ (Geyer 2011). For all parameters of the five parabolas, $\hat{R} = 1.00$ and $N_{\rm eff} \gg 1000$, meaning that convergence was achieved. Marginalized posterior distributions of the fitting parameters and their covariances are provided in Appendix C, together with their median values and uncertainties.

Coloured lines in the top panel of Fig. 5 show the median MCMC predictions for the data. Grouping by N_C explains much of the observed scatter between the points. Residuals (bottom panel of the same Figure) show that some substructure remains. Because absorption system models were all derived from the same spectral data, their χ^2 values are not expected to scatter completely randomly, and the remaining substructure may be irrelevant. Alternatively, there may be an additional contribution to the scatter, beyond the one attributable to N_C, for example model non-uniqueness.

4.2 Constraining $\mathcal{R}$ using χ^2

Substituting equation (5) into (4) and normalizing, the probability density function (PDF) and the cumulative probability density function (CDF) can be calculated analytically from:

$$\mathrm{PDF}(\mathcal{R}, \mathcal{R}_{\rm min}, a) = \sqrt{\tfrac{a}{2\pi}} \exp\left(-\tfrac{a}{2}(\mathcal{R} - \mathcal{R}_{\rm min})^2\right), \quad (6)$$

$$\mathrm{CDF}(\mathcal{R}, \mathcal{R}_{\rm min}, a) = \tfrac{1}{2}\left[1 + \mathrm{erf}\left(\sqrt{\tfrac{a}{2}}(\mathcal{R} - \mathcal{R}_{\rm min})\right)\right]. \quad (7)$$

Fig. 6 shows the results for the PDF (left column) and the CDF (right column) derived from 25 000 different parameter combinations obtained from the MCMC calculations in Section 4.1. The first five rows relate to the five data subsets. The last row shows the average of the first five weighted by the number of values in each subset, N_m.

$N_C = 10$ case provides the most stringent constraints on $\mathcal{R}$, followed by $N_C = 11$, 13, 14 and 12 (in that order). For three subsets ($N_C = 10$, 11, and 13), PDFs are well localized and indicate a statistically significant measurement. Modes of the five curves fall within $^{12}C/^{13}C = 17.4$ to 41.9, in good agreement with each other (when compared to the width of their PDFs). PDFs of $N_C = 12$ and 14 permit the broadest range of solutions, including $^{12}C/^{13}C > 1000$. Plotting a subset of $N_C = 12$ and 14 curves (not shown) we identified some which yielded results consistent with the remaining three subsets. Future, improved, data may reveal which ones are correct. Our results here indicate that the probability of $^{12}C/^{13}C < 100$ is 99.86 per cent, 98.43 per cent, 71.17 per cent, 92.44 per cent and 80.44 per cent (from $N_C = 10$ to 14, respectively). The combined PDF (last row, left column) is well localized with a mode at $^{12}C/^{13}C = 27.3$ and the combined probability that $^{12}C/^{13}C < 100$ is 86.48 per cent. Some other statistical properties, including percentiles and lower limits, are summarized in Table 4.

4.3 Constraining $\mathcal{R}$ using SpIC

In the preceding Section, we used χ^2 as the basis for computing likelihood values. An alternative statistical approach is to instead use an information criterion (Burnham & Anderson 2002), in this case SpIC. We carried out tests, replicating the procedure used for the χ^2 results shown in Table 4. The preliminary indication was that, provided sample subdivision is used, the results do not change significantly. If sample subdivision is not used, the tighter grouping for the SpIC measurements (see Fig. 3) suggests that the SpIC values yield better constraints on $^{12}C/^{13}C$. We also note that Bayesian Model Averaging could also be applied using an information criterion likelihood approach. This would offer the simplification of deriving one numerical result from the entire suite of AI-VPFIT models. However, preliminary calculations suggested a strong weighting towards lowest SpIC models, giving an overly stringent result, which we preferred to avoid in this context.

5 DISCUSSION

5.1 Comparison with previous measurements

The result reported here is $^{12}C/^{13}C = 28.5^{+51.5}_{-10.4}$. Carswell et al. (2011) reported a conservative lower limit of $^{12}C/^{13}C > 5$ (2σ CL) in this DLA. Looking at their fig. 2, ^{13}C was found only in their component N2 (at -17 km s^{-1} in Fig. 1), even though N2 appears (in their spectrum) significantly weaker than component N1 (at -33 km s^{-1} in Fig. 1). However, our higher resolution ESPRESSO data revealed that their component N1 is actually a blend of several absorption features. No significant substructure is seen for their component N2 in the ESPRESSO spectrum, which also appears as the strongest feature in the absorption complex. The new ESPRESSO data therefore explain why ^{13}C seemed to arise in the weaker absorption component in the Carswell et al. (2011) analysis. Interestingly, their reported ratio between column densities of ^{12}C and ^{13}C in N2 equates to $^{12}C/^{13}C = 19^{+20}_{-10}$, in agreement with our findings. Considering that the inferred column densities are close to the linear part of the curve of growth, this agreement is not surprising.

Only three other ^{13}C quasar absorption measurements currently exist. Two recent values are: Noterdaeme et al. (2017) constrained $^{12}C/^{13}C > 40$ at $z_{\rm abs} = 2.525$ and Welsh et al. (2020) constrained $^{12}C/^{13}C > 2.3$ at $z_{\rm abs} = 2.34$. Another seemingly more stringent result is quoted in Levshakov et al. (2006), who measured $^{12}C/^{13}C > 80$ (2σ CL) at $z_{\rm abs} = 1.15$, although an independent re-analysis of the same data did not support such a high value and instead found $^{12}C/^{13}C > 22$ (Carswell et al. 2011). Table 4 provides our analogous 2σ lower limit, 14.6, i.e. all quasar results to date appear consistent.

5.2 Chemical evolution models

^{12}C is formed in the triple-α process during hydrostatic helium-burning and is a primary product of stellar nucleosynthesis. The stable ^{13}C isotope is produced in the hydrogen-burning shell when the CN cycle converts pre-existing ^{12}C into ^{13}C via proton capture followed by β decay. As a star evolves off the main-sequence, the outer convective envelope expands inwards into the CN-cycle-processed regions producing a mixing episode which is called the 'first dredge-up', which lowers the $^{12}C/^{13}C$ (Iben & Renzini 1984). Mixing also occurs in the thermal pulses of intermediate-mass stars that become asymptotic giant branch (AGB) stars. This could lead to a CN-cycle equilibrium ratio of about $^{12}C/^{13}C \sim 4$. These low values ratios are indeed observed in some red supergiants (Lambert & Sneden 1977).

Due to the secondary nature of ^{13}C, chemical evolution models predict a monotonic decrease in the isotopic ratio $^{12}C/^{13}C$ with time (Romano & Matteucci 2003; Kobayashi et al. 2020). This is supported by observations in young molecular clouds for which $^{12}C/^{13}C \sim 60 - 70$, lower than the solar ratio of $^{12}C/^{13}C = 91 \pm 1.3$ (Goto et al. 2003; Ayres et al. 2013). $^{12}C/^{13}C$ is also below solar value in the Galactic centre (Halfen, Woolf & Ziurys 2017) and measurements in the Galaxy support a gradient with galactocentric

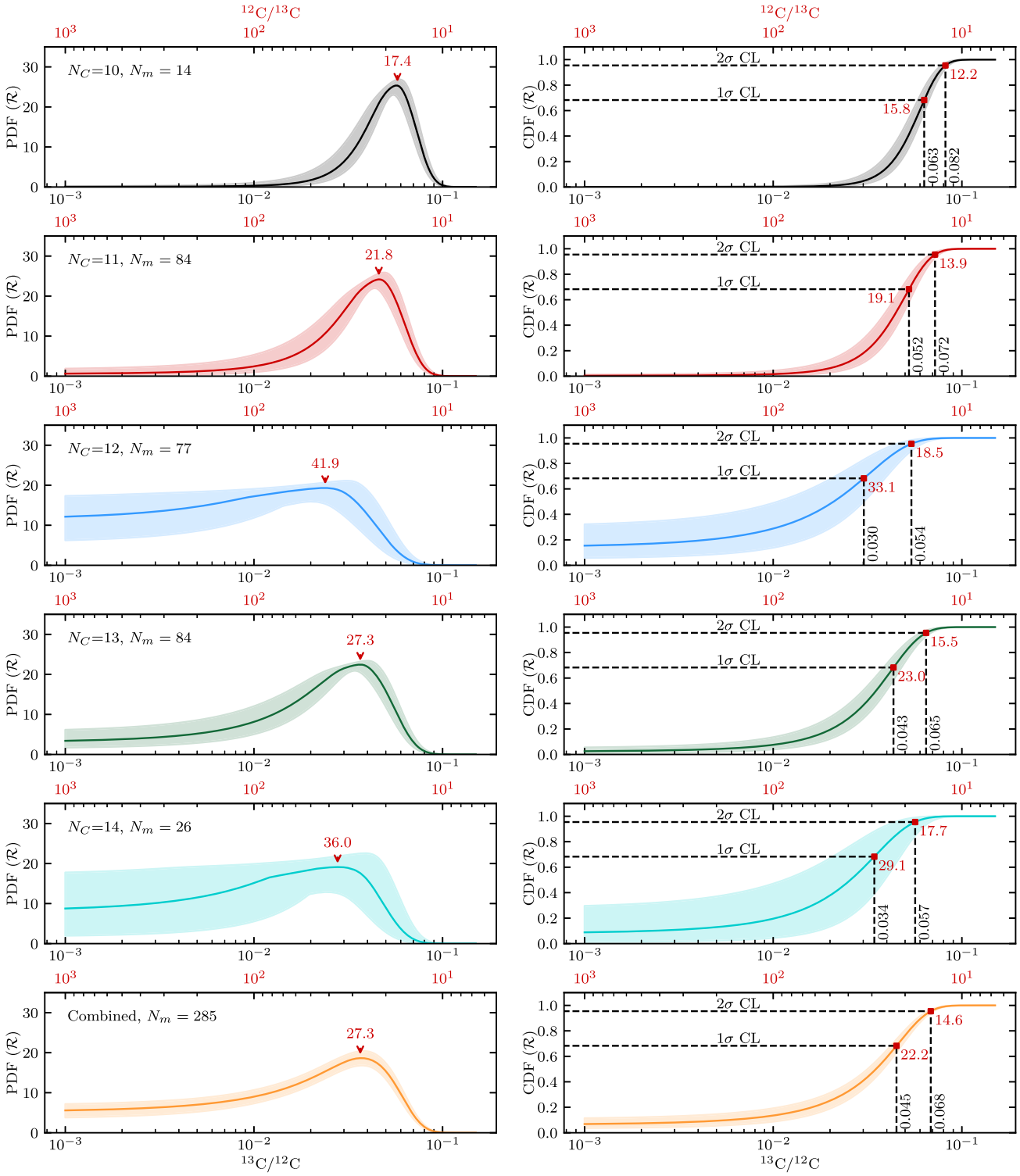

Figure 6. PDF($\mathcal{R}$), left, and CDF($\mathcal{R}$), right, for the five data subsets and the full data set. Each row shows one subset of the data, with the inset specifying N_C and the number of models contained in the subset, N_m. The combined PDF and CDF (final row) are averages of the five above weighted by N_m. In all panels, the thick coloured line is the median over parabola parameters derived by MCMC, and the shaded bands enclose the central 68 per cent of the possible curves. In the panels showing the PDF, the red arrow with a number on top indicates the most probable ^{12}C/^{13}C (the mode of the distribution). In the panels showing the CDF, the horizontal dashed black lines show the probabilities corresponding to 1σ and 2σ confidence limits. Red squares show where those lines intersect the CDF, and the vertical dashed black lines show the corresponding ^{13}C/^{12}C, printed in black. The red numbers adjacent to the red squares are their inverse, i.e. the ^{12}C/^{13}C. Ticks in the bottom with black labels show the ^{13}C/^{12}C, and ticks on the top with red labels show ^{12}C/^{13}C.

Table 4. $^{12}C/^{13}C$ measurement summary. The first column indicates data subset (N_C or combined). The second column gives the most probable value for $^{12}C/^{13}C$ for each case, i.e. the mode of the PDF. The following three columns provide percentile values for $^{12}C/^{13}C$. The ultimate two columns give lower stae2056$_i eqn262.gif\sigma$ (68.27 per cent probability) and 2σ (95.45 per cent probability) confidence limits on $^{12}C/^{13}C$, derived from the CDFs. Note, although we use the σ terminology here, it is clear from Fig. 6 that the uncertainties are not Gaussian.

Subset	Mode	Percentiles			CL	
		16th	50th	84th	1σ	2σ
10	17.4	14.1	17.9	24.7	15.8	12.2
11	21.8	16.4	22.3	34.9	19.1	13.9
12	41.9	24.8	47.8	693.5	33.1	18.5
13	27.3	19.1	28.5	56.5	23.0	15.5
14	36.0	22.8	39.0	133.5	29.1	17.7
Combined	27.3	18.1	28.5	80.0	22.2	14.6

distance (Yan et al. 2023). All of the above is consistent with the secondary nature of ^{13}C. For the reasons above, $^{12}C/^{13}C$ is predicted to be higher than solar at low metallicities (Romano & Matteucci 2003; Fenner, Murphy & Gibson 2005; Kobayashi et al. 2020; Romano 2022). Unfortunately, only a few observations are available in this regime and the results are controversial. Botelho et al. (2020) found a mild increase in the range $-0.2 < [Fe/H] < 0$ in a sample of solar twins, opposite to what is expected if ^{13}C is a secondary element. On the other hand, Crossfield et al. (2019) measured $^{12}C/^{13}C = 296 \pm 45$ and 224 ± 26 in the two components of the brown dwarf system GJ 745 at $[Fe/H] = -0.48$. In some unmixed giants $^{12}C/^{13}C$ is lower than the solar value (Spite et al. 2005) and in the metal-poor star HD 140283, $^{12}C/^{13}C = 33^{+12}_{-6}$ (Spite, Spite & Barbuy 2021). Moreover, very low values of $^{12}C/^{13}C$ have been derived for several CEMP-no stars (carbon enhanced metal-poor stars with $[Ba/F] < 0$) with metallicities lower than $[Fe/H] \lesssim -4$ (Molaro et al. 2023). At very low metallicities the disagreement with the theoretical expectations is striking since values of several thousands are foreseen due to an initial ^{13}C close to zero. Internal production and chemical transfer from a possible massive companion have been ruled out, so the ^{13}C enhancement must originate from their progenitors.

At very low metallicities, mixing between the H- and He-burning zones could be driven by rapid rotation leading to a production of ^{13}C (Meynet, Ekström & Maeder 2006; Chiappini et al. 2008; Limongi & Chieffi 2018). Significant quantities of ^{13}C are expected from massive, low-metallicity, fast-rotating stars with $^{12}C/^{13}C$ between 30 and 300 (Chiappini et al. 2008). Processes necessary to produce ^{13}C are similar to those invoked to explain the primary N behaviour at very low metallicities in other DLAs (Molaro 2003; Zafar et al. 2014).

No stellar $^{12}C/^{13}C$ measurements are available at the metallicity of DLA studied here ($[Fe/H] = -1.27$; Berg et al. 2015) so no direct comparison is possible. Our robust lower limit ($^{12}C/^{13}C > 14.6$, 2σ CL) is consistent with both theoretical predictions and low metallicity measurements. On the other hand, the weighted value we obtained ($^{12}C/^{13}C = 28.5$, see Table 4) is consistent with the measurement in the star HD 140 283 at $[Fe/H] \approx -2.6$, but much lower than that of GJ 745 at $[Fe/H] = -0.48$. If our measured value in the DLA studied here is typical of gas with metallicity of $[Fe/H] \approx -1.2$, it would imply there is a significant and early production of ^{13}C that must necessarily cease to allow $^{12}C/^{13}C$ to reach the measured values at $[Fe/H] \approx -0.5$.

6 SUMMARY

In this work, we have carried out a detailed AI-VPFIT study of the $z_{abs} = 1.776$ DLA towards QSO B1331+170 for a $^{12}C/^{13}C$ measurement. The spectral data are very high quality and hence expected to substantially tighten previous error bars for this system. However, perhaps unsurprisingly, the higher ESPRESSO spectral resolution detected structure that had previously been unresolved, such that the new measurement constraints were not as anticipated.

The use of AI-VPFIT permitted us to generate multiple independent models. This means that, for the first time in this context, we have been able to take into account measurement errors associated with model non-uniqueness (Section 3.4). Our weighted final result (Section 4.2) is $^{12}C/^{13}C = 28.5^{+51.5}_{-10.4}$ (see Table 4 and Fig. 6), a marginal ^{13}C detection. Additional ESPRESSO or new ArmazoNes high Dispersion Echelle Spectrograph (ANDES, Marconi et al. 2022, 2024) or Giant Magellan Telescope - Consortium Large Earth Finder (G-CLEF, Szentgyorgyi et al. 2018) observations may lead to more stringent constraints in the future.A further caveat is that our AI-VPFIT analysis required the $^{12}C/^{13}C$ to be the same in all components. Spatial $^{12}C/^{13}C$ variations could be present within the absorption complex, so our result represents the mean value over the system.

Finally, as mentioned in Section 3.2, we have assumed constant b-parameters for both ^{12}C and ^{13}C. Since the atomic masses are so similar, modelling the system using thermal broadening is impractical, as numerical instabilities would be introduced into the modelling process. If the overall line-broadening contains a thermal contribution, the slightly different atomic masses means our assumption is not quite correct. The maximum impact of this approximation equates to a systematic 4 per cent of the overall b-parameter. The best fractional uncertainty of any b in the absorption complex we measured is slightly below this value, which means the constant-b approximation may impose a slight systematic if there is a significant contribution to thermal broadening. However, the direction of this potential small systematic is such that our lower limit on $^{12}C/^{13}C$ would increase, that is our quoted final result is perhaps slightly conservative.

ACKNOWLEDGEMENTS

The authors acknowledge the ESPRESSO project team for its effort and dedication in building the ESPRESSO instrument as well as the teams who developed software used for the analysis – NUMPY (Harris et al. 2020), SCIPY (Virtanen et al. 2020), MATPLOTLIB (Hunter 2007), NUMPYRO (Phan et al. 2019), JAX (Bradbury et al. 2018), and JAXOPT (Blondel et al. 2021). This work was performed on the OzSTAR national facility at Swinburne University of Technology. The OzSTAR programme receives funding in part from the Astronomy National Collaborative Research Infrastructure Strategy (NCRIS) allocation provided by the Australian Government, and from the Victorian Higher Education State Investment Fund (VHESIF) provided by the Victorian Government. The INAF authors acknowledge financial support of the Italian Ministry of Education, University, and Research with PRIN 201278X4FL and the 'Progetti Premiali' funding scheme. PJ is funded by the Austrian Science Fund (FWF): F6811-N36 within the SFB F68 'Tomography Across the Scales'. MTM acknowledges the support of the Australian Research Council through Future Fellowship grant FT180100194. TMS acknowledges the support from the SNF synergia grant CRSII5-193689 (BLUVES). This work was financed by Portuguese funds through FCT (Fundação para a Ciência e a Tecnologia) in the framework of the project 2022.04048.PTDC (Phi in the Sky, DOI 10.54499/2022.04048.PTDC). CJM also

acknowledges FCT and POCH/FSE (EC) support through Investigador FCT Contract 2021.01214.CEECIND/CP1658/CT0001 (DOI 10.54499/2021.01214.CEECIND/CP1658/CT0001). JIGH and ASM acknowledge the financial support from the Spanish Ministry of Science and Innovation (MICINN) project PID2020-117493GB-I00. We acknowledge financial support from the Agencia Estatal de Investigación of the Ministerio de Ciencia e Innovación MCIN/AEI/10.13039/501100011033 and the ERDF 'A way of making Europe' through project PID2021-125627OB-C32, and from the Centre of Excellence 'Severo Ochoa' award to the Instituto de Astrofisica de Canarias. NCS is co-funded by the European Union (ERC, FIERCE, 101052347). Views and opinions expressed are however those of the author(s) only and do not necessarily reflect those of the European Union or the European Research Council. Neither the European Union nor the granting authority can be held responsible for them. This work was supported by FCT through national funds and by FEDER through COMPETE2020 – Programa Operacional Competitividade e Internacionalização by these grants: UIDB/04434/2020; UIDP/04434/2020. SGS acknowledges the support from FCT through Investigador FCT contract number CEECIND/00826/2018 and POPH/FSE (EC).

DATA AVAILABILITY

Based on observations collected at the European Southern Observatory under ESO programmes 1102.A-0852(C), 106.218R.002, 109.2335.002, and 111.24NH.002 (PI for all programmes is Paolo Molaro) as a part of the ESPRESSO Guaranteed Time Observations. Unprocessed observations are available through the ESO Archive. Spectra and AI-VPFIT models produced as a part of this work are provided as supplementary online material.

REFERENCES

Akaike H., 1974, IEEE Trans. Autom. Control, 19, 716
Ayres T. R., Lyons J. R., Ludwig H. G., Caffau E., Wedemeyer-Böhm S., 2013, ApJ, 765, 46
Bainbridge M. B., Webb J. K., 2017a, Universe, 3, 34
Bainbridge M. B., Webb J. K., 2017b, MNRAS, 468, 1639
Baldwin J. A., Burbidge E. M., Hazard C., Murdoch H. S., Robinson L. B., Wampler E. J., 1973, ApJ, 185, 739
Berg T. A. M., Ellison S. L., Prochaska J. X., Venn K. A., Dessauges-Zavadsky M., 2015, MNRAS, 452, 4326
Blondel M., Berthet Q., Cuturi M., Frostig R., Hoyer S., Llinares-López F., Pedregosa F., Vert J.-P., 2021, preprint (arXiv:2105.15183)
Botelho R. B., Milone A. d. C., Meléndez J., Alves-Brito A., Spina L., Bean J. L., 2020, MNRAS, 499, 2196
Bozdogan H., 1987, Psychometrika, 52, 345
Bradbury J. et al., 2018, JAX: composable transformations of Python+NumPy programs, accessed 29 August 2024, http://github.com/google/jax
Burnham K., Anderson D., 2002, Model Selection and Multimodel Inference: A Practical Information-theoretic Approach. Springer Verlag, New York
Carswell R. F., 2023, VPFIT homepage, accessed 29 August 2024, https://people.ast.cam.ac.uk/ rfc/
Carswell R. F., Webb J. K., 2014, Astrophysics Source Code Library, record ascl:1408.015
Carswell R. F., Hilliard R. L., Strittmatter P. A., Taylor D. J., Weymann R. J., 1975, ApJ, 196, 351
Carswell R. F., Jorgenson R. A., Wolfe A. M., Murphy M. T., 2011, MNRAS, 411, 2319
Caughlan G. R., 1965, ApJ, 141, 688
Chiappini C., Ekström S., Meynet G., Hirschi R., Maeder A., Charbonnel C., 2008, A&A, 479, L9
Crossfield I. J. M. et al., 2019, ApJ, 871, L3
Cui J., Bechtold J., Ge J., Meyer D. M., 2005, ApJ, 633, 649
Dekker H., D'Odorico S., Kaufer A., Delabre B., Kotzlowski H., 2000, in Iye M., Moorwood A. F., eds, Proc. SPIE Conf. Ser. Vol. 4008, Optical and IR Telescope Instrumentation and Detectors. SPIE, Bellingham, p.534
Fenner Y., Murphy M. T., Gibson B. K., 2005, MNRAS, 358, 468
Geyer C., 2011, in Brooks Steve, Gelman Andrew, Jones Galin, Meng Xiao-Li, eds, Introduction to Markov Chain Monte Carlo. CRC Press, Boca Raton, Florida, USA, p. 3
Goldbach C., Nollez G., 1987, A&A, 181, 203
Goto M. et al., 2003, ApJ, 598, 1038
Halfen D. T., Woolf N. J., Ziurys L. M., 2017, ApJ, 845, 158
Haridass C., Huber K. P., 1994, ApJ, 420, 433
Harris C. R. et al., 2020, Nature, 585, 357
Henkel C., Downes D., Weiß A., Riechers D., Walter F., 2010, A&A, 516, A111
Henkel C. et al., 2014, A&A, 565, A3
Horne K., 1986, PASP, 98, 609
Hunter J. D., 2007, Comput. Sci. Eng., 9, 90
Hurvich C. M., Tsai C.-L., 1989, Biometrika, 76, 297
Iben I., Renzini A., 1984, Phys. Rep., 105, 329
Kimble R. A. et al., 1998, ApJ, 492, L83
Kobayashi C., Karakas A. I., Umeda H., 2011, MNRAS, 414, 3231
Kobayashi C., Karakas A. I., Lugaro M., 2020, ApJ, 900, 179
Lai K.-F., Ubachs W., De Oliveira N., Salumbides E. J., 2020, Atoms, 8, 62
Lambert D. L., Sneden C., 1977, ApJ, 215, 597
Lee C.-C., Webb J. K., Carswell R. F., Milaković D., 2021a, MNRAS, 504, 1787
Lee C.-C., Webb J. K., Milaković D., Carswell R. F., 2021b, MNRAS, 507, 27
Lee C.-C., Webb J. K., Carswell R. F., Dzuba V. A., Flambaum V. V., Milaković D., 2023, MNRAS, 521, 850
Levshakov S. A., Centurión M., Molaro P., Kostina M. V., 2006, A&A, 447, L21
Li Z. S., Lundberg H., Berzinsh U., Johansson S., Svanberg S., 2000, J. Phys. B: At. Mol. Phys., 33, 5593
Limongi M., Chieffi A., 2018, ApJS, 237, 13
Marconi A. et al., 2022, in Evans C. J., Bryant J. J., Motohara K., eds, Proc. SPIE Conf. Ser. Vol. 12184, Ground-based and Airborne Instrumentation for Astronomy IX. SPIE, Bellingham, p.1218424
Marconi A. et al., 2024, preprint (arXiv:2407.14601)
Meyer D. M., York D. G., Black J. H., Chaffee F. H. J., Foltz C. B., 1986, ApJ, 308, L37
Meynet G., Ekström S., Maeder A., 2006, A&A, 447, 623
Modigliani A., Sosnowska D., Lovis C., 2023, ESPRESSO Pipeline User Manual version 3.0.0. accessed 29 August 2024,https://ftp.eso.org/pub/dfs/pipelines/instruments/espresso/espdr-pipeline-manual-3.0.0.pdf, accessed 29 August 2024
Molaro P., 2003, in Charbonnel C., Schaerer D., Meynet G., eds, ASP Conf. Ser. Vol. 304, CNO in the Universe. Astron. Soc. Pac., San Francisco, p.221
Molaro P. et al., 2023, A&A, 679, A72
Muller S., Guélin M., Dumke M., Lucas R., Combes F., 2006, A&A, 458, 417
Murphy M., 2018, MTMurphy77/UVES_popler: UVES_popler: POst-PipeLine Echelle Reduction software, Zenodo, doi:10.5281/zenodo.1297190
Murphy M. T., Kacprzak G. G., Savorgnan G. A. D., Carswell R. F., 2019, MNRAS, 482, 3458
Murphy M. T. et al., 2022, A&A, 658, A123
Noterdaeme P. et al., 2017, A&A, 597, A82
Pasquini L., Milaković D., 2024, preprint (arXiv:2405.14955)
Pepe F. et al., 2021, A&A, 645, A96
Phan D., Pradhan N., Jankowiak M., 2019, preprint (arXiv:1912.11554)
Prantzos N., Aubert O., Audouze J., 1996, A&A, 309, 760

Robertson J. G., 1986, PASP, 98, 1220
Romano D., 2022, A&A Rev., 30, 7
Romano D., Matteucci F., 2003, MNRAS, 342, 185
Schmidt T. M. et al., 2021, A&A, 646, A144
Songaila A. et al., 1994, Nature, 371, 43
Spite M. et al., 2005, A&A, 430, 655
Spite M., Spite F., Barbuy B., 2021, A&A, 652, A97
Strittmatter P. A., Carswell R. F., Burbidge E. M., Hazard C., Baldwin J. A., Robinson L., Wampler E. J., 1973, ApJ, 183, 767
Szentgyorgyi A. et al., 2018, in Evans C. J., Simard L., Takami H., eds, Proc. SPIE Conf. Ser. Vol. 10702, Ground-based and Airborne Instrumentation for Astronomy VII. SPIE, Bellingham, p.107021R
Vehtari A., Gelman A., Simpson D., Carpenter B., Bürkner P.-C., 2021, Bayesian Analysis, 16, 667
Virtanen P. et al., 2020, Nat. Methods, 17, 261
Vogt S. S. et al., 1994, in Crawford D. L., Craine E. R., eds, Proc. SPIE Conf. Ser. Vol. 2198, Instrumentation in Astronomy VIII. SPIE, Bellingham, p.362
Wallström S. H. J., Muller S., Guélin M., 2016, A&A, 595, A96
Webb J. K., Lee C.-C., Carswell R. F., Milaković D., 2021, MNRAS, 501, 2268
Webb J. K., Lee C.-C., Milaković D., 2022, Universe, 8, 266
Welsh L., Cooke R., Fumagalli M., Pettini M., 2020, MNRAS, 494, 1411
Wiescher M., Görres J., Uberseder E., Imbriani G., Pignatari M., 2010, Annu. Rev. Nucl. Part. Sci., 60, 381
Yan Y. T. et al., 2023, A&A, 670, A98
Zafar T., Centurión M., Péroux C., Molaro P., D'Odorico V., Vladilo G., Popping A., 2014, MNRAS, 444, 744
Zechmeister M., Anglada-Escudé G., Reiners A., 2014, A&A, 561, A59

SUPPORTING INFORMATION

Supplementary data are available at *MNRAS* online.

online_supplementary_material

Please note: Oxford University Press is not responsible for the content or functionality of any supporting materials supplied by the authors. Any queries (other than missing material) should be directed to the corresponding author for the article.

APPENDIX A: EXAMPLE MODELS

The figures in this Appendix show four example AI-VPFIT models, each with a different $^{12}C/^{13}C$, derived as a part of the analysis presented in the main text. Fig. A1 shows the same model as is shown in Fig. 1 ($^{12}C/^{13}C = 28.14$), but with spectra separated by epoch. The remaining Figures show models with $^{12}C/^{13}C = 20$ (Fig. A2), solar $^{12}C/^{13}C$ (= 91, Fig. A3), and $^{12}C/^{13}C = 500$ (Fig. A4).

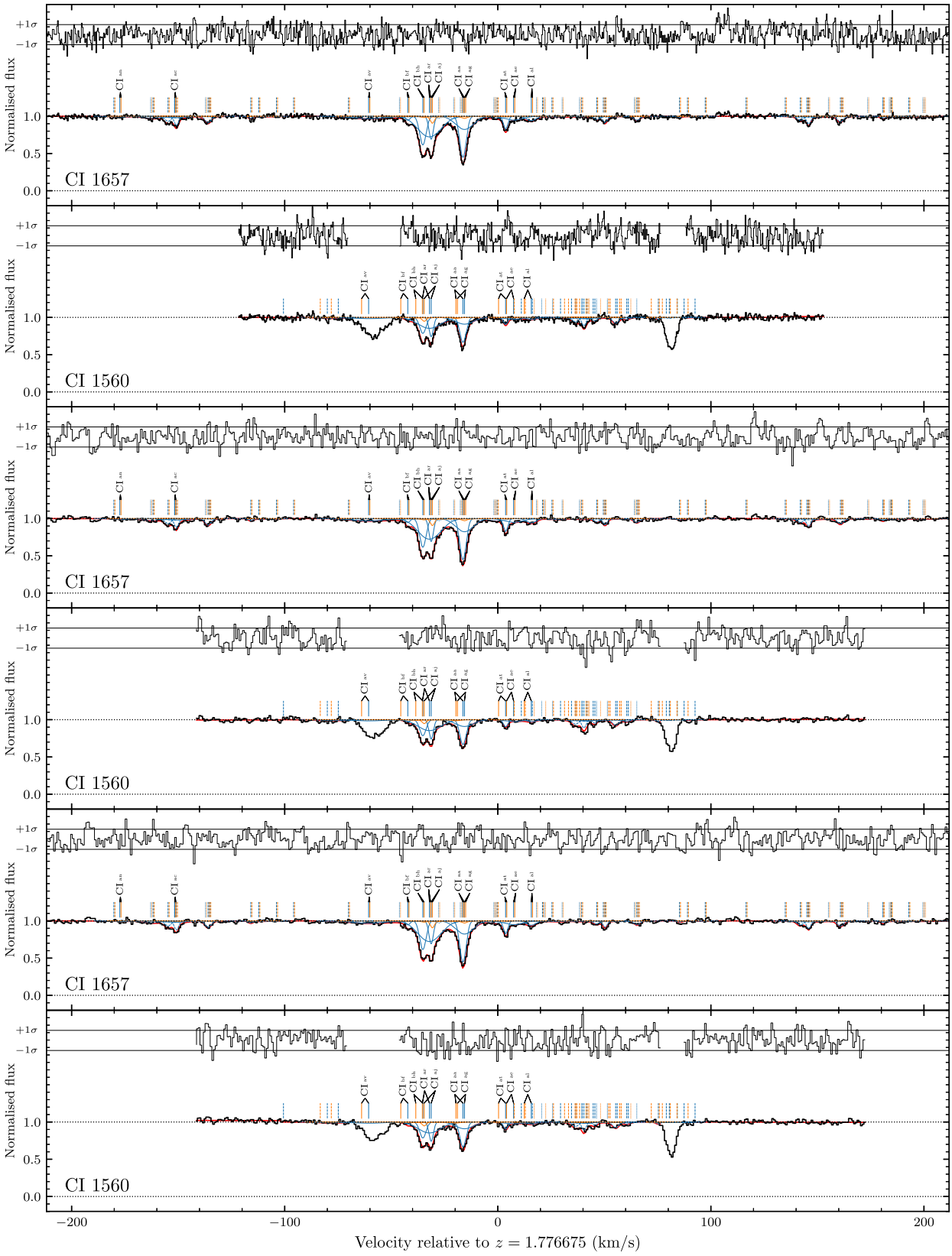

Figure A1. The same as Fig. 1 but spectra of the three epochs are shown separately. First two rows are epoch I, second two rows are epoch II, and the final two rows are epoch III. $\chi^2_\nu = 0.6362$.

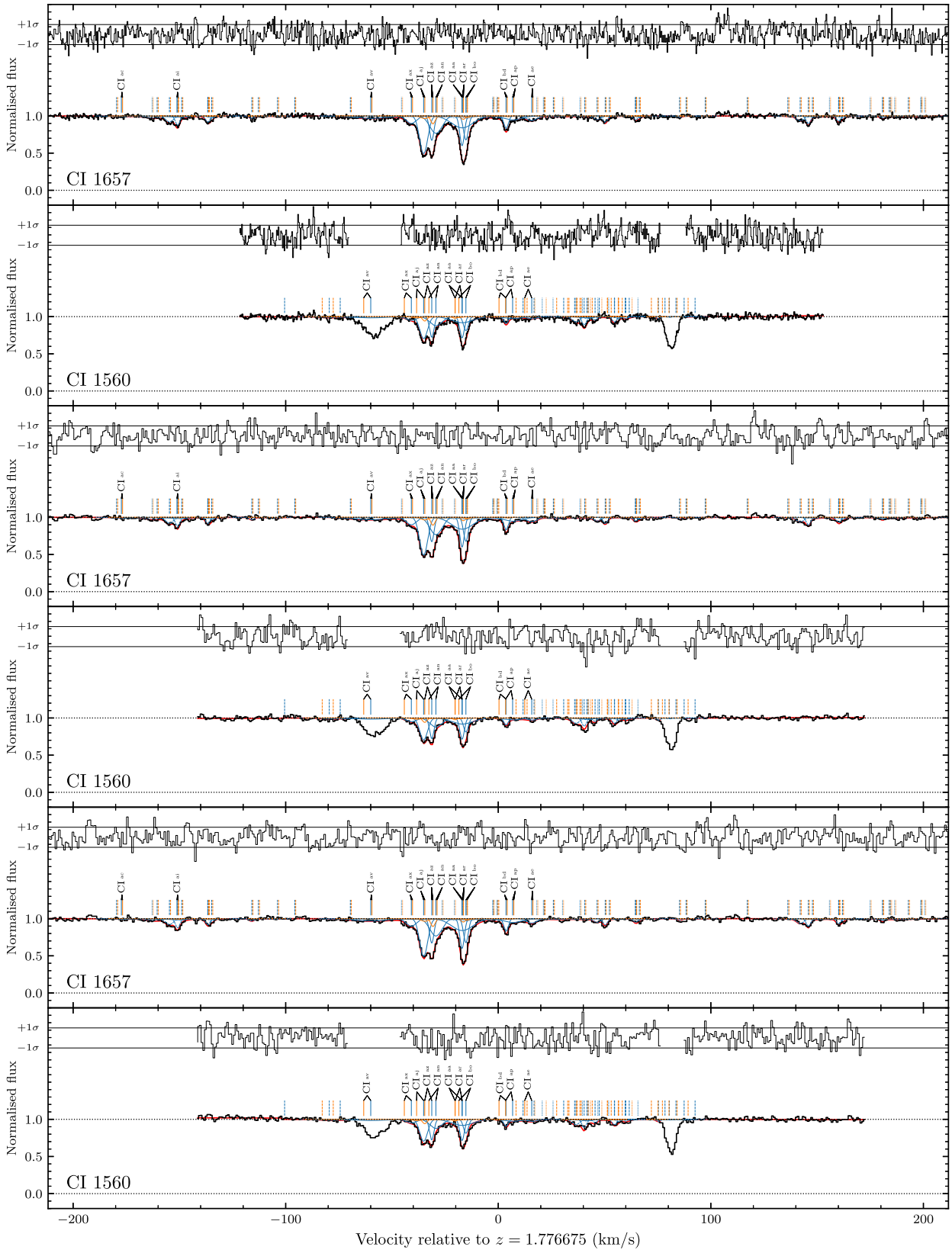

Figure A2. The same as Fig. A1 but for $^{12}C/^{13}C = 20$. $\chi^2_\nu = 0.6269$.

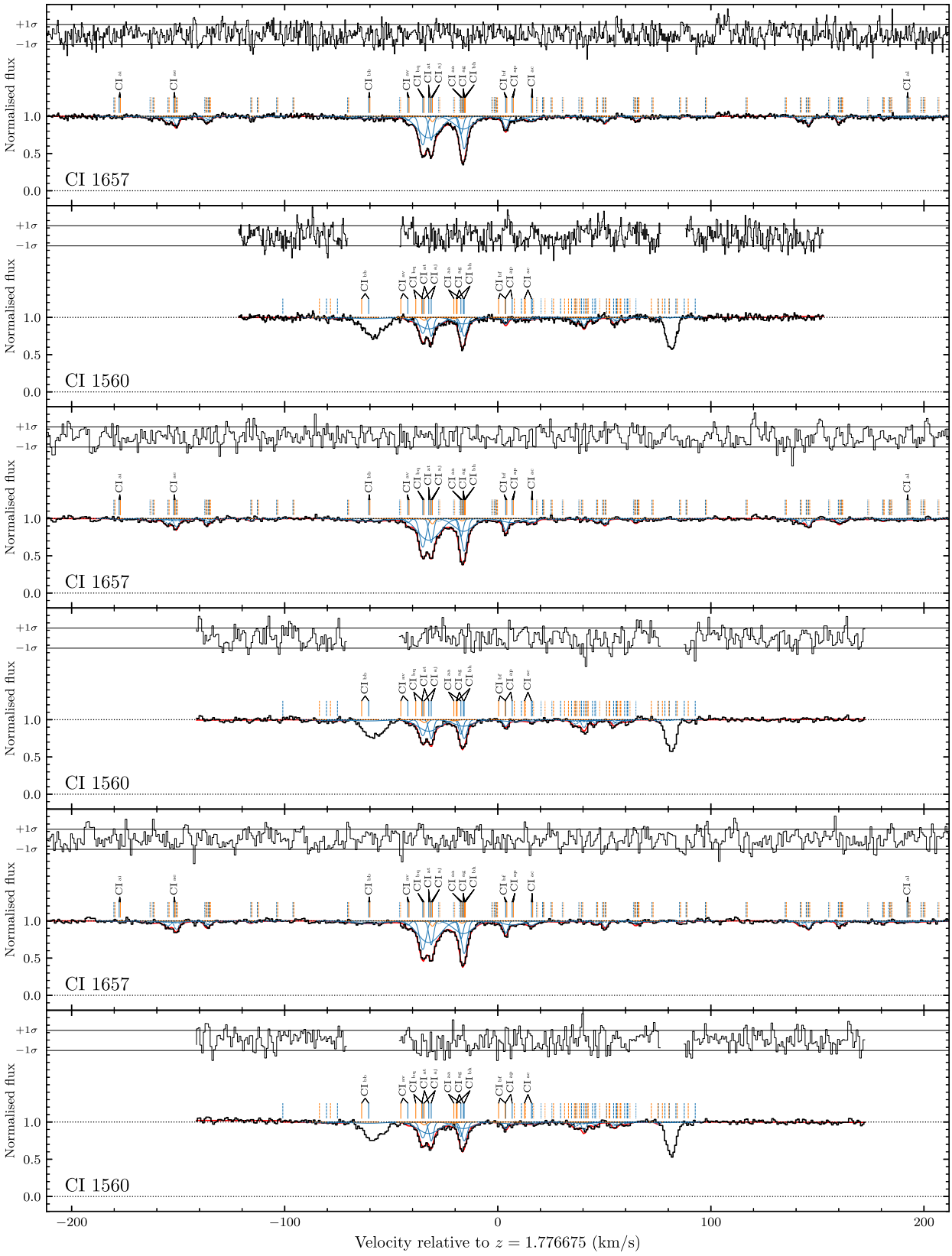

Figure A3. The same as Fig. A1 but for $^{12}C/^{13}C = 90.71$. $\chi^2_\nu = 0.6216$.

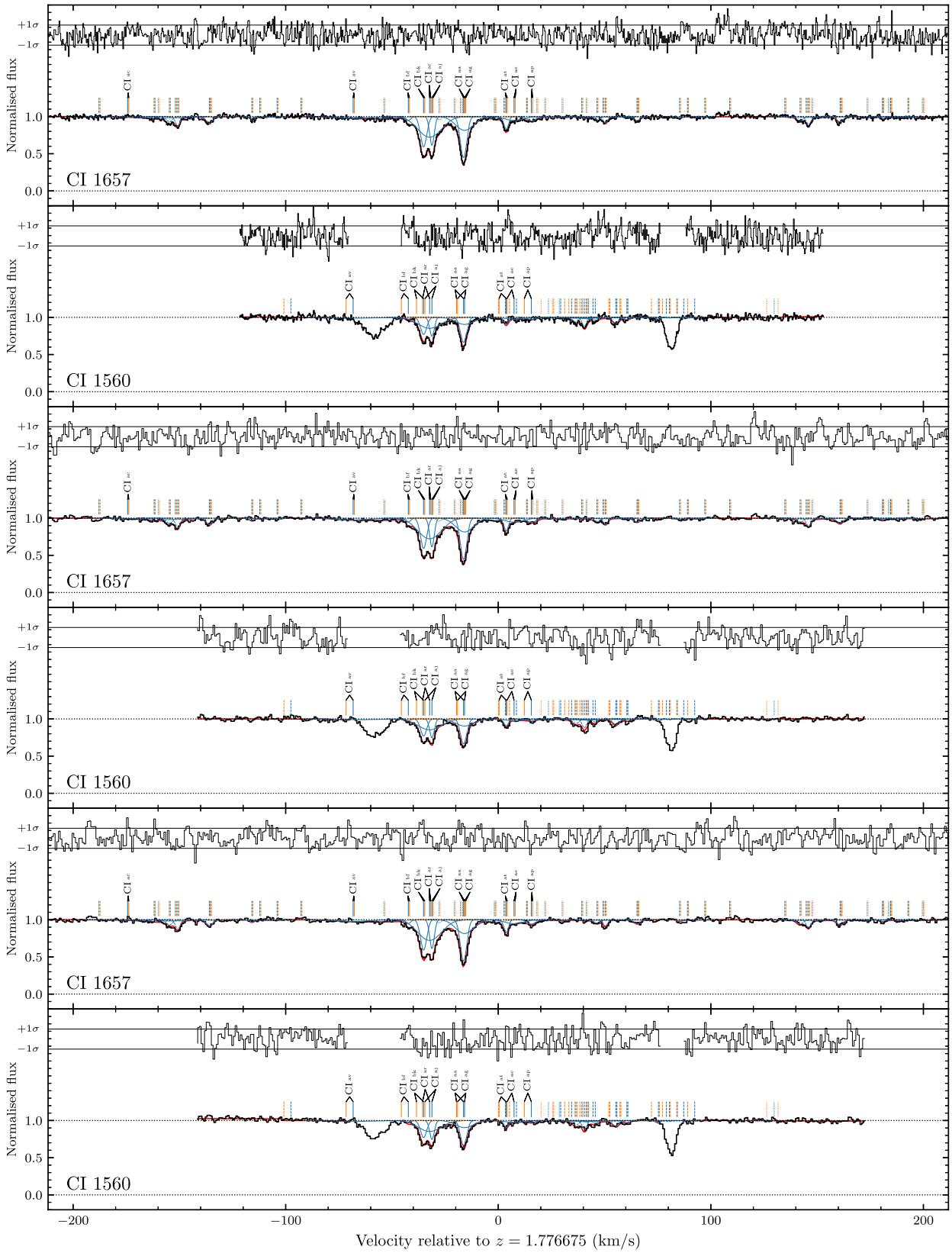

Figure A4. The same as Fig. A1 but for $^{12}C/^{13}C = 500$. $\chi^2_\nu = 0.6448$.

APPENDIX B: COMPARING ESPRESSO C I VELOCITY STRUCTURE WITH INDEPENDENT MODELS FROM H_2

Cui et al. (2005) analysed H rotational levels seen in the data collected using Space Telescope Imaging Spectrograph (STIS) on the *Hubble Space Telescope* (Kimble et al. 1998) associated with the DLA studied here. Assuming a single velocity component for H_2, a population analysis of its rotational levels yielded a H_2 gas temperature of $T = 152 \pm 10$ K. Subsequently, Carswell et al. (2011) examined the physical properties of the gas in more detail by combining the same STIS observations of H_2 with Ultraviolet and Visible Echelle Spectrograph (UVES, Dekker et al. 2000) and High Resolution Echelle Spectrometer (HIRES, Vogt et al. 1994) observations covering the wavelength ranges containing heavy element absorption. In the Carswell et al. (2011) analysis, 52 H_2 rotational levels seen in the STIS data were modelled together with five C I transitions from UVES and HIRES, assuming three velocity components for both H_2 and C I. Only two components had reliably measured temperatures, $T(H_2) = 86^{+14}_{-10}$ K, and 177^{+30}_{-22} K (at $z_{abs} = 1.7763702$ and 1.7765246, i.e. their components N1 and N2, respectively). A lower limit of $T(H_2) \gtrsim 200$ K was obtained for a component at $z_{abs} = 1.7767176$ (their N3′). Carswell et al. (2011) suggested N3′ to be a blend of several more narrow features that are unresolved in their data. They also suggested that N2 is mostly thermally broadened whereas N1 and N3′ are dominated by turbulent motions. The best estimate for the kinetic temperature of component N2 provided by Carswell et al. (2011) is $T = 218$ K, from C I line broadening.

Out of the 285 surviving AI-VPFIT models produced in this work, 281 contain C I components with b-parameters consistent with temperatures $T \leqslant 218$ K. 26 models have one, 129 models have two, 112 models have three, 11 models have four, and 3 models have five such components. Fig. B1 shows where those components tend to fall within the absorption complex. The three most prominent narrow components are found at $z_{abs} = 1.7763856$ (C1, at -31.2 km s^{-1} in Fig. B1), $z_{abs} = 1.7765156$ (C2, at -17.2 km s^{-1}), and $z_{abs} = 1.7767093$ (C3, at $+3.7$ km s^{-1}). The redshifts of the C1 and C2 are 1.7 and 1.0 km s^{-1} away from the redshifts of N1 and N2 reported by Carswell et al. (2011). Such shifts are not surprising, considering that ESPRESSO data allowed for resolving more structure compared to previous UVES and HIRES observations ($R = 42000$ and 48000, respectively, compared to ESPRESSO's $R = 140000$). Component C3 was not known before.

We next derived the temperatures of C1, C2, and C3 assuming that their broadening is only due to thermal gas motions. In doing that, we considered components that are $\leq \pm 0.5$ km s^{-1} away from their redshifts (see above), and have b-parameters corresponding to a maximum ^{12}C gas temperature of 1000 K ($b = 1.18$ km s^{-1}). Median temperatures obtained this way are $T(C1) = 51^{+124}_{-27}$ K, $T(C2) = 60^{+12}_{-48}$ K, and $T(C3) = 180^{+159}_{-50}$ K. The quoted errors correspond to the 16th and the 84th percentiles.

Identifying our C1 with N1 from Carswell et al. (2011), we found the temperature derived from the ESPRESSO C I line widths ($T = 51^{+124}_{-27}$ K) to be in agreement with the temperature derived from H_2 by Carswell et al. (2011) ($T = 86^{+14}_{-10}$ K). While it may appear that temperature obtained by us for C2 ($T = 60^{+12}_{-48}$ K) is in disagreement with the temperature Carswell et al. (2011) reported for N2 ($T = 177^{+30}_{-22}$ K), this is not the case, as ESPRESSO data revealed the presence of several components not resolved in the lower resolution UVES and HIRES data used by Carswell et al. (2011). Additional ESPRESSO observations may be used to confirm the presence of cold components at -42, -36, -34, and -15 km s^{-1} (with respect to $z = 1.7766750$) contained in some AI-VPFIT models. Observations using even higher spectral resolution spectrographs (such as G-CLEF, with a planned $R = 300\,000$; Szentgyorgyi et al. 2018), would also be useful.

Parameter constraints in our calculations required $b < 10$ km s^{-1}, an empirically guided value. We note that some models reveal the presence of broad components i.e. with b-parameters near or at the upper limit. It is unavoidably the case that there may be clumps of blended lines that cannot be resolved (given the intrinsic line properties and spectral resolution). The number of free parameters in our models are decided on by an information criterion, giving the benefit of reproducibility. Given the constraints imposed, statistically the data do not justify additional parameters. Examining where components with $b \geq 8$ km s^{-1} fall within the absorption complex, we found them to be concentrated at the following locations: at -175 (14 per cent of all broad components), -87 (1 per cent), -72 (2 per cent), -64 (44 per cent), -34 (1 per cent), -16 (≤ 1 per cent),

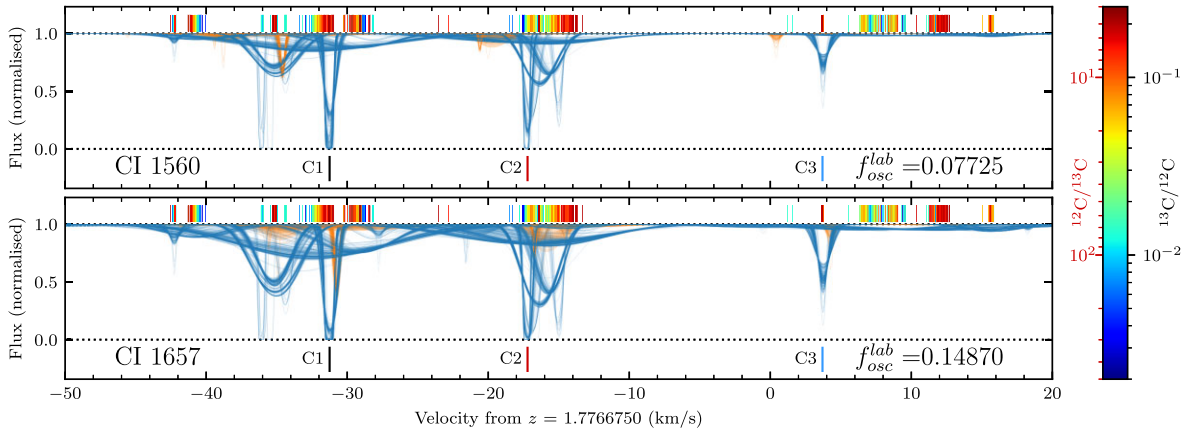

Figure B1. Theoretical absorption system models before convolution with the assumed IPs. The models and the colour coding are the same as in Fig. 4. A single AI-VPFIT model may contain between zero and five narrow ($b < 0.55$ km s^{-1}) velocity components, with most models containing two of them. The three most prominent narrow components are at -31.2 km s^{-1} (C1), -17.2 km s^{-1} (C2), and $+3.7$ km s^{-1} (C3). The redshifts and temperatures of C1 and C2 are in agreement with literature reported redshifts of H_2 absorption and their temperatures (Carswell et al. 2011), but AI-VPFIT derived them completely independently and without instructions. The presence of C3 was previously unknown.

+9 (8 per cent), +13 (15 per cent), and +194 km s^{-1} (15 per cent). Two of the strong C I components from which $^{12}C/^{13}C$ constraint is derived are C1 and C2 (see Fig. B1), i.e. the overwhelming majority (> 98 per cent) of the broad components are located far from regions providing constraints on $^{12}C/^{13}C$.

APPENDIX C: MCMC POSTERIORS

Fig. C1 shows the marginalized posterior distributions for parameters included in MCMC calculations presented in Section 4, and their mutual covariances.

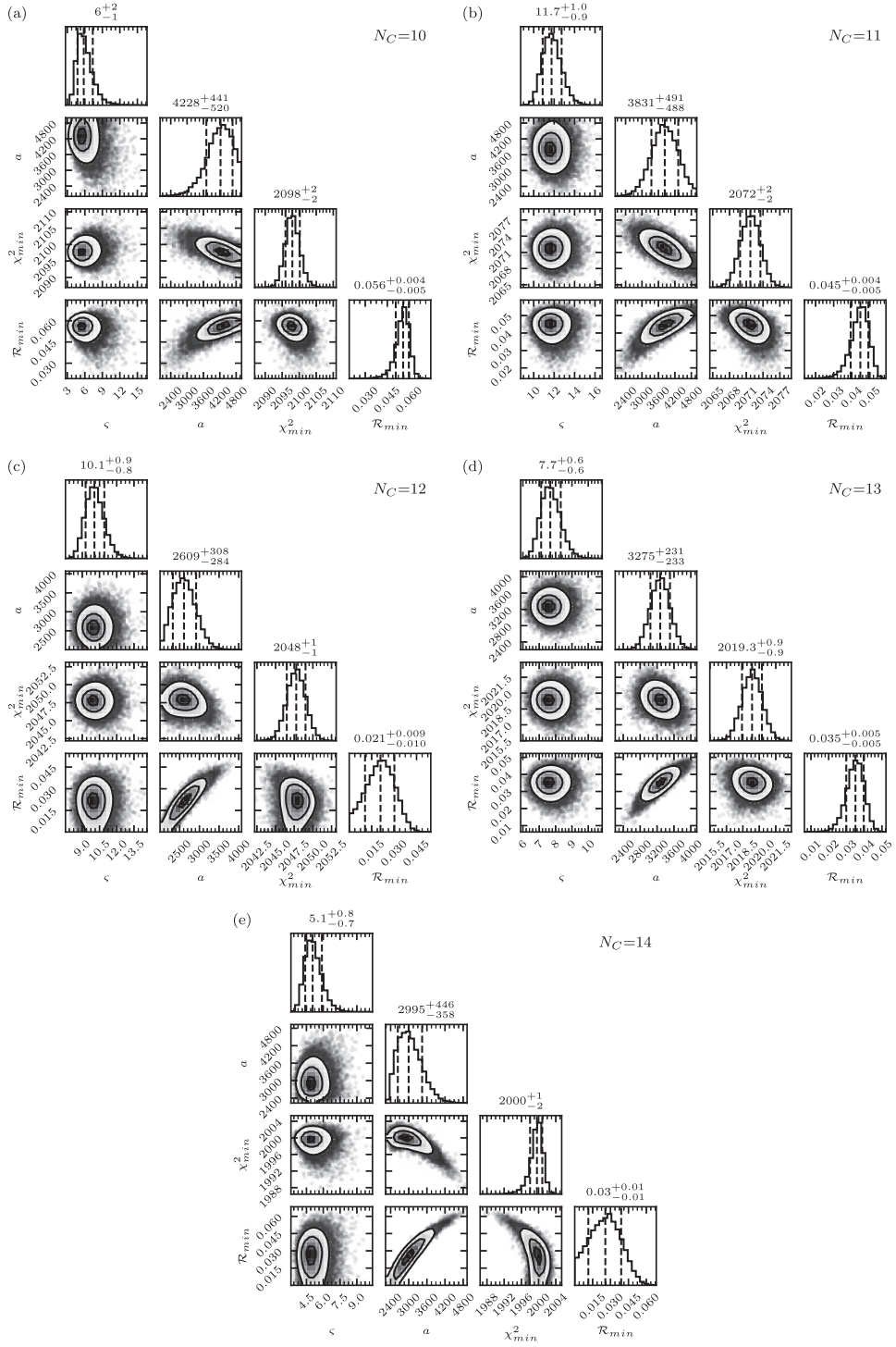

Figure C1. Posterior distributions and covariances of equation (5) parameters after MCMC optimization for the five data subsets (panels a–e). N_C for each subset is indicated in the top right corner of each panel. Numbers are the median and the central 68 per cent limits, indicated by the dashed lines.

This paper has been typeset from a TEX/LATEX file prepared by the author.